

Determination of Land and Ocean Reflective, Radiative, and Biophysical Properties Using Multi-angle Imaging

John V. **Martonchik**, David J. Diner,
Mail Stop 169-237
Jet Propulsion Laboratory, California Institute of Technology
4800 Oak Grove Drive
Pasadena, CA 91109, USA

Bernard Pinty, **Michel** M. Verstraete
Space Applications Institute, EC Joint Research Centre
I-2 1020 Ispra (VA), Italy

Ranga B. Myneni, Yuri **Knyazikhin**
Department of Geography, Boston University
Boston MA 02215, USA

Howard R. Gordon
Department of Physics, University of Miami
Coral Gables, FL 33124, USA

Submitted to: *IEEE Transactions on Geoscience and Remote Sensing*
November. 1997

ABSTRACT

Knowledge of the directional and hemispherical reflectance properties of natural surfaces such as soils and vegetation canopies is essential for classification studies and canopy model inversion. The Multi-angle Imaging SpectroRadiometer (**MISR**), an instrument to be launched in 1998 onboard the **EOS-AM1** platform, will make global observations of the Earth's surface at 1.1 km spatial resolution with the objective of determining the atmospherically corrected reflectance properties of most of the land surface and the tropical ocean. The algorithms to retrieve surface directional reflectance, **albedos**, and selected **biophysical** parameters using MISR data are described. Since part of the **MISR** data analyses includes an aerosol retrieval, it **is** assumed that the optical properties of the atmosphere (i.e., aerosol characteristics) have been determined **well** enough to accurately model the radiative transfer process. The core surface retrieval algorithms are tested on simulated MISR data, computed using realistic surface reflectance and aerosol models, and the sensitivity of the retrieved directional and hemispherical reflectance to aerosol type and column amount is illustrated. Included is a summary list of the **MISR** surface products.

I. INTRODUCTION

About 30% of the Earth's surface is covered by land and much of this is vegetated. Thus, land surface processes are important components of the terrestrial climate system [1]. The bulk of the solar energy provided to the troposphere transits through the lower boundary (oceans and continents) first and is made available to the atmosphere through the fluxes of sensible, latent, and thermal radiation. Accurate descriptions of the interaction of surface vegetation and atmospheric processes require quantitative information on fluxes of energy (radiation transfer) and mass (water vapor and CO₂) which are strong functions of photosynthetic and evapotranspiration rates. These, in turn, are strongly correlated with surface hemispherical reflectance (i.e., albedo) [2]-[4]. Therefore, accurate hemispherical reflectance estimates are expected to be diagnostic of the influence of biophysical processes on surface-atmosphere interactions. These estimates are also important, even over non-vegetated terrain, because modifications to the surface, through natural or human-induced causes, will potentially change the hemispherical reflectance, and consequently, impact the climate system as a result of perturbing the lower boundary condition [5]-[7].

Angular signature information is also expected to be a significant component of improved surface cover classification and characterization [8]. The time-evolution of terrestrial ecosystems is difficult to monitor at the surface and satellite platforms provide a unique opportunity to carry out extensive surveys with comprehensive spatial coverage and high time resolution. Detection of **ecophysiological** change on the land surface, resulting from natural processes (canopy succession and species replacement) or **anthropogenic** activities (e.g., deforestation, acid rain), necessitates accurate, repeatable measurements of the surface that can be used for landscape classification. Over oceans, monitoring of ocean color provides the means of monitoring marine biological productivity and its changes with time.

In an effort to meet these observational needs, the Multi-angle Imaging SpectroRadiometer (**MISR**), scheduled for launch in 1998 on the **EOS-AM 1** platform, is capable of continuously imaging the Earth's surface at nine fixed viewing angles (70.5°, 60.0°, 45.6°, 26.1° forward and aftward of nadir, and nadir) and four spectral bands (446, 558, 672, and 866 nm) [9]. Thus, a given scene will be observed at these view angles and wavelengths within a span of only 7 minutes, i.e., near simultaneously, allowing the assumption that the cloud-free atmosphere over the scene remains constant during the course of the measurements. The MISR surface retrievals will be performed at the spatial resolution of 1.1 km globally, termed a subregion, but localized areas of interest can be processed at **MISR's** highest resolution of 275 m.

H. SURFACE RETRIEVAL STRATEGY

Before surface retrievals can be performed within a given region, various atmospheric parameters need to be determined by means of an aerosol retrieval. Here, a region is defined to be an area 17.6 km x 17.6 km in size, composed of 16 x 16 1.1 km subregions, covering either land or ocean. However, an aerosol retrieval is not performed if the region exhibits too much cloudiness or if the surface terrain is too topographically complex. Even if an aerosol retrieval was successful, some 1.1 km subregions within the region may not be suitable for a surface retrieval due to cloudiness, cloud shadows, sun glitter (usually over water), or instrument-related reasons.

The following sequence of land surface retrieval activity is performed on all suitable subregions. First, the hemispherical-directional reflectance factor (H_{DRF}) for all available camera view angles and the bihemispherical reflectance (**BHR**) are determined in the four **MISR** spectral bands. The H_{DRF} , a measure of the view-angle-dependent surface-leaving radiance, and the **BHR**, an al-

bedo, are surface reflectance properties for illumination conditions of the ambient atmosphere (i.e., direct and diffuse sunlight) and are retrieved with a minimum number of assumptions. These parameters are directly related to radiances and fluxes at the surface and, therefore, provide information to radiation balance studies of the atmosphere/surface system. Using the HDRF as a starting point, the corresponding bidirectional reflectance factor (**BRF**) and the directional-hemispherical reflectance (**DHR**) are determined. The BRF and the DHR are equivalent surface properties to the HDRF and BHR, respectively, but assume only direct sunlight illumination in the absence of an atmosphere. Therefore, the BRF can be retrieved from an HDRF only if a BRF model is assumed, making the BRF and DHR somewhat more model-dependent than the HDRF and the BHR. By using a parametrized BRF model, however, and determining the model parameters, the possibility exists of extrapolating the retrieved BRF and DHR to other view angles and sun angles not obtainable by **MISR**.

From the spectral **BHR** and **DHR** a PAR-integrated BHR and DHR are obtained. The PAR (photosynthetically active radiation) band covers the 400-700 nm wavelength range. The **PAR**-integrated BHR and DHR are a measure of the amount of PAR absorbed by the surface (vegetative and non-vegetative) under ambient and direct illumination conditions, respectively. The fractional amount of incident PAR absorbed by vegetation canopies (**FPAR**) only (and not the understory) and the canopy leaf area index (**LAI**) are then estimated using the retrieved spectral surface products (**BHR**, **DHR**, **BRF**, **HDRF**) as input to detailed radiative transfer models of various plant canopy biome types. The details of the **LAI/FPAR** algorithm can be found in [10].

The ocean surface retrieval process is performed only for the tropical ocean, which for our purpose is contained within a 600 km wide band centered on the equator. Phytoplankton pigment concentration is estimated, using the retrieved water-leaving radiances in the **MISR** blue (446 nm) and green (558 nm) bands as input to a modified Coastal Zone Color Scanner (**CZCS**) algorithm. However, these water-leaving radiances are retrieved in two distinct ways. One is the conventional approach, essentially employing the **MODIS/SeaWiFS** algorithm [11], [12] which has its own collection of aerosol models, and the other is based on the **MISR** aerosol and **HDRF** retrieval algorithms. Pigment concentrations are determined using both sets of water-leaving radiances for later comparison studies.

111. SURFACE RETRIEVAL PRELIMINARIES

The algorithms assume that scattering and absorption of sunlight within the atmosphere is adequately described by radiative transfer theory [13]. In general, attenuation of the incident and reflected beams as a result of extinction (scattering and absorption) along the ray path is somewhat offset by diffuse radiation that has been (1) reflected by the atmosphere without reaching the surface, (2) subjected to multiple reflections between the atmosphere and surface, and (3) scattered into the line-of-sight from neighboring areas. The top-of-atmosphere (TOA) radiance depends on both the optical characteristics of the atmosphere and the reflectance properties (spatial, spectral, and angular) of the surface. The solution to the radiative transfer equation is an integral expression which must be solved for the surface reflectance. At the bottom of the atmosphere, the surface is illuminated by radiation which has been both directly and diffusely transmitted through the atmosphere, as well as by backscattered light from the surface. The diffuse radiation field, called skylight, illuminates the surface from all angles in the downward hemisphere. In contrast, directly transmitted sunlight is more or less **uni-directional** (except for the finite angular size of the Sun, which can be ignored for practical purposes).

An implicit assumption of the surface retrieval algorithms is that each of the 36 (9 view angles x 4 spectral bands) MISR radiances is associated with the same ground footprint, particularly with regard to size. At the highest resolution, the geometric crosstrack footprint dimension of each camera is virtually the same, about 275 m, as a consequence of the particular camera effective focal length. However, surface projection effects increase the geometric along-track footprint dimension with increasing view angle. Thus, the along-track instantaneous footprint size of the D (70.0°), cameras at the highest resolution is three times that of the off-nadir A (26.1°) cameras, 707 m versus 236 m, but the along-track sample spacing is still 275 m. When the high resolution samples are averaged 4 x 4 to create a subregion with a crosstrack dimension of 1.1 km, the surface projection effect is substantially mitigated for the subregion along-track dimension, due to the 275 m sample spacing. Thus, subregions from the D, C (60.0°) and B (45.6°) cameras are only 17%, 1170, and 6% geometrically larger, respectively, than subregions from the A cameras. These variations in footprint size are not considered significant and so the common subregions from all nine cameras are treated in the retrieval process as having identical ground footprints.

Because the surface topography is variable within the footprints of the MISR observations, the effects of terrain slope must be considered in the surface retrieval. The primary effects of a sloped or tilted terrain on the observed radiance include the dependence of irradiance (both direct and diffuse), upward transmittance, and possibly surface BRF on the tilt angle (slope). Some of these effects have been studied insofar as how they impact the classification accuracy of forest canopies (e.g., [14], [15]). A more general analysis was done by Woodham and Lee [16], who devised a 6-parameter model of surface reflectance to account for slope effects. Using this model, Gray [17] reported that the classification accuracy for a forested area increased from 51 % (uncorrected Landsat MSS data) to 80% with correction for solar incidence angle providing the largest effect. If, however, the slope is kept under 20°, the atmospheric parameters associated with diffuse scattering seem to depend only slightly on the slope angle [15]. Therefore, surface parameters will be retrieved only for subregions with slopes within the 20° limit, using a topographic mask to filter out more rugged terrain. In this case the MISR surface retrievals do not need to explicitly incorporate tilt or slope effects. Instead, in every 1.1 km land subregion where a retrieval is performed, the surface leaving radiance is considered to transition an imaginary horizontal surface (a surface parallel to the standard Earth ellipsoid) and the MISR surface retrieval results are referenced to this surface. Certain mountainous regions obviously will be excluded from standard product generation activities, but it is expected that they will be investigated on a specialized basis.

Although the adjacency effect is also mentioned in the above cited references, there is presently no operational method to correct for reflections from adjacent, spatially heterogeneous terrain, especially at off-nadir view angles. For spacecraft measurements these adjacency effects can be described by a convolution of the three-dimensional upward transmittance and the surface-leaving radiance. The radiance $L_{\lambda, x, y}^{TOA}$ leaving the top of the atmosphere at wavelength λ and surface spatial coordinates x, y , can be written as

$$\begin{aligned}
 L_{\lambda, x, y}^{TOA}(-\mu, \mu_0, \phi - \phi_0; \tau_\lambda) &= L_{\lambda}^{atm}(-\mu, \mu_0, \phi - \phi_0; \tau_\lambda) + e^{-\tau_\lambda/\mu} \cdot L_{\lambda, x, y}^{surf}(-\mu, \mu_0, \phi - \phi_0; \tau_\lambda) \\
 &+ \int_0^1 \int_0^{2\pi} T_{\lambda, x, y}(-\mu, -\mu', \phi - \phi'; \tau_\lambda) \otimes L_{\lambda, x, y}^{surf}(-\mu', \mu_0, \phi' - \phi_0; \tau_\lambda) d\mu' d\phi'
 \end{aligned} \tag{1}$$

with

$$L_{\lambda, x, y}^{surf}(-\mu, \mu_0, \phi - \phi_0; \tau_\lambda) = \frac{1}{\pi} \int_0^{2\pi} \int_0^\pi R_{\lambda, x, y}(-\mu, \mu', \phi - \phi') L_{\lambda, x, y}^{inc}(\mu', \mu_0, \phi' - \phi_0; \tau_\lambda) \mu' d\mu' d\phi'. \quad (2)$$

Here, μ and μ_0 are the cosines of the view and Sun angles, defined with respect to the normal to the surface ellipsoid (not the **local** topographically-defined surface orientation) and $\phi - \phi_0$ is the view azimuthal **angle** with respect to the Sun position, also in the ellipsoid reference system. The convention $-\mu$ and μ is used for **upwelling** and **downwelling** radiation respectively. The properties of the atmosphere are assumed to be horizontally homogeneous. In (1), L_λ^{atm} is the radiance scattered by the atmosphere to space without interacting with the surface (i.e., the path radiance), $L_{\lambda, x, y}^{surf}$ is the surface-leaving radiance, $T_{\lambda, x, y}$ is the upward diffuse transmittance, and τ_λ is the optical depth of the atmosphere (**Rayleigh** + aerosols). In (2), $L_{\lambda, x, y}^{inc}$ is the direct and diffuse downward radiance incident on the surface, and $R_{\lambda, x, y}$ is the surface bidirectional reflectance factor (**BRF**). The BRF is π times the bidirectional reflectance distribution function (**BRDF**).

In the general 3-D solution to the radiative transfer problem with a horizontally uniform atmosphere over a spatially flat but contrasting surface, the transmittance $T_{\lambda, x, y}$ can be thought of as a point-spread function and the convolution operation \otimes describes the blurring effect of the atmosphere on the surface reflectance $R_{\lambda, x, y}$ [18]. When the image spatial resolution is comparable to or greater than the atmospheric scattering scale height (defined by the vertical distribution of the aerosols and/or **Rayleigh** scattering molecules), adjacency effects are mitigated and (1) reduces to the standard one-dimensional radiative transfer regime, where $T_{\lambda, x, y}$ is effectively a delta function in the spatial coordinates. In this case, (1) simplifies to

$$L_{\lambda, x, y}^{TOA}(-\mu, \mu_0, \phi - \phi_0; \tau_\lambda) = L_\lambda^{atm}(-\mu, \mu_0, \phi - \phi_0; \tau_\lambda) + e^{-\tau_\lambda/\mu} L_{\lambda, x, y}^{surf}(-\mu, \mu_0, \phi - \phi_0; \tau_\lambda) + \int_0^{2\pi} \int_0^\pi T_{\lambda, x, y}(-\mu, -\mu', \phi - \phi'; \tau_\lambda) L_{\lambda, x, y}^{surf}(-\mu', \mu_0, \phi' - \phi_0; \tau_\lambda) d\mu' d\phi' \quad (3)$$

Over ocean the 1-D radiative transfer description of the TOA radiance, described by (3), is appropriate, due mainly to a lack of contrast on the ocean surface. Over land, however, there can be significant surface contrast and aerosol scale heights are about 1- 2 km, comparable to the surface spatial resolution, leading to adjacency effects. Nevertheless, by virtue of the 1.1 -km sub-region size, we assume that (3) is sufficiently accurate such that surface retrievals are not significantly

[y compromised by not using (1). This assumption has been tested using a 3-D radiative transfer algorithm [19], [20] on a scene with a high-contrast boundary (a coastline)[21]. The results of these tests indicate that at the spatial resolution corresponding to unaveraged MISR data (275 m), and especially at high spatial resolution (30 m or finer) obtained with sensors such as the Landsat Thematic Mapper, SPOT, or ASTER, the use of (3) can lead to retrieved surface reflectance with errors larger than those resulting from expected uncertainties in the aerosol retrieval. At the 1.1-km subregion size, however, the errors resulting from the use of 1-D radiative transfer theory are similar in magnitude to errors incurred with the aerosol retrieval. Therefore, until we are confident that aerosol retrieval errors can be minimized, we do not consider the additional complexities of including 3-D radiative transfer theory to be warranted.

Finally, a principal assumption in the surface retrieval process is that the state of the atmosphere is known well enough that the various atmosphere-dependent functions, e.g., T_λ and L_λ^{atm} in (3), can be determined. For MISR this process involves an aerosol retrieval [22] which allows a determination of the atmospheric optical depth (aerosol + Rayleigh) and its scattering properties (phase function and single scattering albedo) in the four MISR spectral bands. This information is then used as input to lookup tables of radiative transfer parameters contained in the Simulated MISR Ancillary Radiative Transfer (SMART) dataset [23]. The use of the SMART dataset is an efficient alternative to real time computations of parameters such as atmospheric path radiance, diffuse transmittance, and irradiance. This dataset is used in the aerosol retrieval process and it also provides the necessary atmospheric quantities in (3), needed by the surface retrieval algorithms.

IV. RETRIEVAL OF HDRF AND BHR

The retrieved HDRF is essentially a measure of surface-leaving radiance at the nine MISR view angles and four spectral bands for the particular sun angle geometry of the observations. Integration of the HDRF over the sky hemisphere results in the BHR or surface albedo for ambient sky illumination. These kinds of data currently are being obtained for very localized areas as part of sporadically timed field experiments, using hand-held radiometers with footprint sizes of less than a meter (see, e.g., [24]). In contrast MISR will provide the HDRF and BHR systematically with a footprint size of 1.1 km over most of the global land surface. The retrieval algorithm described below simultaneously retrieves the spectral HDRF and BHR.

The description of the **HDRF/BHR** retrieval algorithm begins with a mathematical definition of the *hemispherical-directional reflectance factor for non-isotropic incident radiation*, the full descriptor of the HDRF. It can be written as

$$r_{\lambda, x, y}(-\mu, \mu_0, \phi - \phi_0; \tau_\lambda) = \frac{L_{\lambda, x, y}^{surf}(-\mu, \mu_0, \phi - \phi_0; \tau_\lambda)}{\frac{1}{\pi} \int_0^1 \int_0^{2\pi} L_{\lambda, x, y}^{inc}(\mu', \mu_0, \phi' - \phi_0; \tau_\lambda) \mu' d\mu' d\phi'} \quad (4)$$

and is equal to the ratio of the radiance reflected from the surface, $L_{\lambda, x, y}^{surf}$, to the radiance reflected from an ideal **lambertian** target, each with the same beam geometry and illuminated under identical atmospheric conditions. The surface irradiance $E_{\lambda, x, y}$ is defined as

$$E_{\lambda, x, y}(\mu_0; \tau_\lambda) = \int_0^1 \int_0^{2\pi} L_{\lambda, x, y}^{inc}(\mu', \mu_0, \phi' - \phi_0; \tau_\lambda) \mu' d\mu' d\phi', \quad (5)$$

and is the incident flux (or, more precisely, the radiant flux density) at the surface. The total radiance incident on the surface, $L_{\lambda, x, y}^{inc}$, in (5) includes the contribution from all of the multiple reflections between the atmosphere and surface and, therefore, $E_{\lambda, x, y}$ is dependent on the surface BRF, $R_{\lambda, x, y}$.

Another basic radiometric quantity is the radiant exitance at the surface, $M_{\lambda, x, y}$, expressed as

$$M_{\lambda, x, y}(\mu_0; \tau_\lambda) = \int_0^1 \int_0^{2\pi} L_{\lambda, x, y}^{surf}(-\mu, \mu_0, \phi - \phi_0; \tau_\lambda) \mu d\mu d\phi, \quad (6)$$

and is the exiting radiant flux density at the surface.

Now when $r_{\lambda, x, y}$ in (4) is integrated over the hemisphere, the result, $A_{\lambda, x, y}^{hem}$, is the *bihemispherical reflectance for non-isotropic incident radiation* or **BHR**, i.e.,

$$\begin{aligned}
A_{\lambda, x, y}^{hem}(\mu_0; \tau_\lambda) &= \frac{1}{\pi} \int_0^1 \int_0^{2\pi} r_{\lambda, x, y}(-\mu, \mu_0, \phi - \phi_0; \tau_\lambda) \mu d\mu d\phi \\
&= \frac{M_{\lambda, x, y}(\mu_0; \tau_\lambda)}{E_{\lambda, x, y}(\mu_0; \tau_\lambda)}
\end{aligned} \tag{7}$$

Thus, the BHR is the ratio of the radiant exitance to the irradiance, i.e., the albedo.

The surface-dependent irradiance $E_{\lambda, x, y}$ is related to the black surface irradiance $E_{\lambda, b}$ via the highly accurate approximation

$$E_{\lambda, x, y}(\mu_0; \tau_\lambda) = \frac{E_{\lambda, b}(\mu_0; \tau_\lambda)}{1 - A_{\lambda, x, y}^{hem}(\mu_0; \tau_\lambda) \cdot s_\lambda(\tau_\lambda)} \tag{8}$$

where s_λ is the bottom-of-atmosphere (BOA) bihemispherical albedo. Combining (7) and (8), the expression for $A_{\lambda, x, y}^{hem}$ then can be rewritten as

$$A_{\lambda, x, y}^{hem}(\mu_0; \tau_\lambda) = \frac{M_{\lambda, x, y}(\mu_0; \tau_\lambda)}{E_{\lambda, b}(\mu_0; \tau_\lambda) + s_\lambda(\tau_\lambda) \cdot M_{\lambda, x, y}(\mu_0; \tau_\lambda)}. \tag{9}$$

Also, using (5) and (8), $r_{\lambda, x, y}$ can be rewritten as

$$r_{\lambda, x, y}(-\mu, \mu_0, \phi - \phi_0; \tau_\lambda) = \frac{\pi \cdot L_{\lambda, x, y}^{surf}(-\mu, \mu_0, \phi - \phi_0; \tau_\lambda) \cdot [1 - A_{\lambda, x, y}^{hem}(\mu_0; \tau_\lambda) \cdot s_\lambda(\tau_\lambda)]}{E_{\lambda, b}(\mu_0; \tau_\lambda)}. \tag{10}$$

Thus, when $L_{\lambda, x, y}^{surf}$ is known, $r_{\lambda, x, y}$ and $A_{\lambda, x, y}^{hem}$ can be computed from (6), (9), and (10). The other parameters in these equations, the black surface irradiance $E_{\lambda, b}$, the BOA bihemispherical albedo s_λ , and the atmospheric optical depth τ_λ , depend only on atmospheric properties and are determined in the aerosol retrieval process.

The integral equation (3) can be solved for $L_{\lambda, x, y}^{surf}$ by starting with an initial estimate and converging to the solution via iteration. An initial estimate, $L_{\lambda, x, y}^{(0)}$, is made by using (3), but with $L_{\lambda, x, y}^{surf}$ in the diffuse transmittance term brought outside the integral. Then, we can write

$$L_{\lambda, x, y}^{surf(0)}(-\mu, \mu_0, \phi - \phi_0; \tau_\lambda) = \frac{L_{\lambda, x, y}^{MISR}(-\mu, \mu_0, \phi - \phi_0) - L_{\lambda}^{atm}(-\mu, \mu_0, \phi - \phi_0; \tau_\lambda)}{e^{-\tau_\lambda/\mu} + t_\lambda(-\mu; \tau_\lambda)} \quad (11)$$

where

$$t_\lambda(-\mu; \tau_\lambda) = \int_0^{12\pi} \int_0 T_\lambda(-\mu, -\mu', \phi - \phi'; \tau_\lambda) d\mu' d\phi', \quad (12)$$

and $L_{\lambda, x, y}^{MISR}$ is identified with the TOA radiance $L_{\lambda, x, y}^{* \circ \lambda}$. The iteration algorithm for $L_{\lambda, x, y}^{surf}$ is also derived from (3),

$$L_{\lambda, x, y}^{surf(n+1)}(-\mu, \mu_0, \phi - \phi_0; \tau_\lambda) = [L_{\lambda, x, y}^{MISR}(-\mu, \mu_0, \phi - \phi_0) - L_{\lambda}^{atm}(-\mu, \mu_0, \phi - \phi_0; \tau_\lambda)] \cdot e^{\tau_\lambda/\mu} - \left[\int_0^{12\pi} \int_0 T_\lambda(-\mu, -\mu', \phi - \phi'; \tau_\lambda) L_{\lambda, x, y}^{surf(n)}(-\mu', \mu_0, \phi' - \phi_0; \tau_\lambda) d\mu' d\phi' \right] \cdot e^{\tau_\lambda/\mu} \quad (13)$$

Note that (13) implies that $L_{\lambda, x, y}^{surf}$ is directly determined only at the nine Sun-view angles of the MISR observations, but evaluation of the last term requires that $L_{\lambda, x, y}^{surf}$ be known over a complete hemisphere. However, we can obtain a good approximation of this integral if both T_λ and $L_{\lambda, x, y}^{surf(n)}$ are described by a two term cosine series in azimuth angle. Then, (13) can be rewritten as

$$L_{\lambda, x, y}^{surf(n+1)}(-\mu, \mu_0, \phi - \phi_0; \tau_\lambda) = [L_{\lambda, x, y}^{MISR}(-\mu, \mu_0, \phi - \phi_0) - L_{\lambda}^{atm}(-\mu, \mu_0, \phi - \phi_0; \tau_\lambda)] \cdot e^{\tau_\lambda/\mu} - 2\pi \cdot e^{\tau_\lambda/\mu} \int_0^l T_{\lambda, 0}(-\mu, -\mu'; \tau_\lambda) L_{\lambda, 0, x, y}^{surf(n)}(-\mu', \mu_0; \tau_\lambda) d\mu' - \pi \cos(\phi - \phi_0) \cdot e^{\tau_\lambda/\mu} \int_0^l T_{\lambda, 1}(-\mu, -\mu'; \tau_\lambda) L_{\lambda, 0, x, y}^{surf(n)}(-\mu', \mu_0; \tau_\lambda) d\mu' \quad (14)$$

where

$$L_{\lambda, x, y}^{surf(n)}(-\mu, \mu_0, \phi - \phi_0; \tau_\lambda) = L_{\lambda, 0, x, y}^{surf(n)}(-\mu, \mu_0; \tau_\lambda) + L_{\lambda, 1, x, y}^{surf(n)}(-\mu, \mu_0; \tau_\lambda) \cdot \cos(\phi - \phi_0) \quad (15)$$

$$T_\lambda(-\mu, -\mu_0, \phi - \phi_0; \tau_\lambda) = T_{\lambda, 0}(-\mu, -\mu_0; \tau_\lambda) + T_{\lambda, 1}(-\mu, -\mu_0; \tau_\lambda) \cdot \cos(\phi - \phi_0) \quad (16)$$

Then,

$$L_{\lambda, 0, x, y}^{surf(n)}(-\mu, \mu_0; \tau_\lambda) = \frac{1}{[\cos(\phi_f - \phi_0) - \cos(\phi_a - \phi_0)]} \cdot [L_{\lambda, x, y}^{surf(n)}(-\mu, \mu_0, \phi_a - \phi_0; \tau_\lambda) \cos(\phi_f - \phi_0) - L_{\lambda, x, y}^{surf(n)}(-\mu, \mu_0, \phi_f - \phi_0; \tau_\lambda) \cos(\phi_a - \phi_0)] \quad (17)$$

$$L_{\lambda, 1, x, y}^{surf(n)}(-\mu, \mu_0; \tau_\lambda) = \frac{L_{\lambda, x, y}^{surf(n)}(-\mu, \mu_0, \phi_f - \phi_0; \tau_\lambda) - L_{\lambda, x, y}^{surf(n)}(-\mu, \mu_0, \phi_a - \phi_0; \tau_\lambda)}{\cos(\phi_f - \phi_0) - \cos(\phi_a - \phi_0)}, \quad (18)$$

where ϕ_f and ϕ_a are the forward and aftward view azimuth angles of each symmetrically viewing camera pair. Thus, $L_{\lambda, 0, x, y}^{surf(n)}$ and $L_{\lambda, 1, x, y}^{surf(n)}$ can be calculated for the five unique MISR view zenith angles, 70.5° , 60.0° , 45.6° , 26.10° , and 0° . To perform the integrations in (14), these quantities then are interpolated to the Radau quadrature points at which $T_{\lambda, 0}$ and $T_{\lambda, 1}$ are evaluated. These transmittance coefficients are another product of the aerosol retrieval process and precomputed values are contained in the SMART dataset.

At every iteration step the BHR $A_{\lambda, x, y}^{hem(n)}$ is evaluated using (9) with $M_{\lambda, x, y}$ from (6), rewritten as

$$M_{\lambda, x, y}^{(n)}(\mu_0; \tau_\lambda) = 2\pi \int_0^1 L_{\lambda, 0, x, y}^{refl(n)}(-\mu, \mu_0; \tau_\lambda) \mu d\mu. \quad (19)$$

The iteration process is terminated when the condition,

$$\frac{|A_{\lambda, x, y}^{hem(n)}(\mu_0; \tau_\lambda) - A_{\lambda, x, y}^{hem(n-1)}(\mu_0; \tau_\lambda)|}{A_{\lambda, x, y}^{hem(n)}(\mu_0; \tau_\lambda)} \leq \epsilon, \quad (20)$$

is satisfied. The configurable parameter ϵ is set to 0.01.

The procedure described by (14) is very fast and very stable, usually requiring three iterations or less to achieve convergence. Once the iteration is finished (10) is used to evaluate the HDRF, $r_{\lambda, x, y}$.

V. RETRIEVAL OF BRF AND DHR

The algorithm for retrieving the HDRF and BHR from MISR TOA radiances is virtually independent of any particular kind of surface BRF model and is highly accurate when correct atmospheric information is used. Going a step further, it then is possible to retrieve the bidirectional reflectance factor (BRF) and directional-hemispherical reflectance (DHR) from the HDRF by using a parameterized BRF model. The BRF is actually a limiting form of the HDRF, defined for the special condition of no atmosphere. The same limiting form also applies to the relationship between the BHR and the DHR. This implies that there is no diffuse radiation incident on the surface and only the direct radiance from the Sun. It is the removal of the effects of the diffuse radiance from the HDRF which requires the use of a BRF model in the BRF/DHR algorithm and which ultimately makes the retrieved BRF and DHR somewhat model dependent. The BRF/DHR algorithm also determines the BRF surface model parameters, which allows the model to predict the surface angular reflectance properties fully and thus to extend the angular range of the BRF and DHR to also include all solar and view angle geometries not covered by the observations. With further research, it may also be possible to obtain a correlation between the model parameters and surface physical parameters (e.g., LAI and leaf orientation parameters) and surface classification types.

A number of BRF surface models have been proposed in the literature, ranging from those with only 2-3 parameters (e.g., [26]) to those with 10 and more parameters (e.g., [27], [28]). Devising new and better BRF surface models is an ongoing effort by many researchers and there is no consensus at the present time as to an optimum BRF model for use with multi-angle data. Different researchers may want to use different models, depending on the focus of their investigations. If simple models, containing two or three parameters, are used in the inversion process then the retrieved HDRF at the nine MISR angles, associated with individual orbital swaths, usually will be a sufficient data set upon which to perform BRF retrievals. However, if the more complicated BRF surface models are used, containing more than three parameters, then the collection of MISR HDRF's, associated with overlapping swaths from multiple orbits and multiple days, will be required. For the MISR at-launch standard product, we have opted for the former strategy and are using a three parameter, semi-empirical BRF model.

The retrieval algorithm starts with the relationship between the HDRF, $r_{\lambda, x, y}$, and the BRF, $R_{\lambda, x, y}$,

$$r_{\lambda, x, y}(-\mu, \mu_0, \phi - \phi_0; \tau_\lambda) = \frac{\int_0^{12\pi} R_{\lambda, x, y}(-\mu, \mu', \phi - \phi') L_{\lambda, x, y}^{inc}(\mu', \mu_0, \phi' - \phi_0; \tau_\lambda) \mu' d\mu' d\phi'}{E_{\lambda, x, y}(\mu_0; \tau_\lambda)} \quad (21)$$

where (2), (4), and (5) were used. Here, $r_{\lambda, x, y}$ and $A_{\lambda, x, y}^{hem}$ have been retrieved previously and the irradiance $E_{\lambda, x, y}$ is computed using (8). The incident radiance $L_{\lambda, x, y}^{inc}$ at the surface is approximated by the form,

$$\begin{aligned} L_{\lambda, x, y}^{inc}(\mu, \mu_0, \phi - \phi_0; \tau_\lambda) &\equiv E_{0, \lambda} e^{-\tau_\lambda / \mu_0} \cdot \delta(\mu - \mu_0) \cdot \delta(\phi - \phi_0) \\ &+ E_{0, \lambda} \cdot [\bar{T}_{\lambda, 0}(\mu, \mu_0; \tau_\lambda) + \bar{T}_{\lambda, 1}(\mu, \mu_0; \tau_\lambda) \cos(\phi - \phi_0)] \\ &+ \frac{A_{\lambda, x, y}^{hem}(\mu_0; \tau_\lambda) \cdot s_\lambda(\tau_\lambda)}{\pi} \cdot E_{\lambda, x, y}(\mu_0; \tau_\lambda) \end{aligned} \quad (22)$$

where δ is the Dirac delta function and $E_{0, \lambda}$ is the TOA solar irradiance. The downward diffuse transmittance \bar{T}_λ is described by a two term cosine series in $\phi - \phi_0$, where the coefficients $\bar{T}_{\lambda, 0}$ and $\bar{T}_{\lambda, 1}$ are defined as in (16) for the upward diffuse transmittance. The first term on the right-hand-side of (22) describes the direct radiance, the second term approximates the diffuse downwelling radiance in the absence of any surface reflectance (i.e., a black surface), and the last term approximates the downwelling radiance due to multiple reflections between the atmosphere and the surface.

There is a reciprocity relationship between the upward and downward diffuse transmittances, namely,

$$\mu \cdot T_\lambda(-\mu, -\mu', \phi - \phi'; \tau_\lambda) = \mu' \cdot \bar{T}_\lambda(\mu', \mu, \phi' - \phi; \tau_\lambda). \quad (23)$$

Substituting (22) for $L_{\lambda, x, y}^{inc}$ in (21) and using (16) and (23),

$$\begin{aligned}
r_{\lambda, x, y}(-\mu, \mu_0, \phi - \phi_0; \tau_\lambda) &\equiv \frac{\mu_0 E_{0, \lambda}}{E_{\lambda, x, y}(\mu_0; \tau_\lambda)} \cdot [e^{-\tau_\lambda / \mu_0} R_{\lambda, x, y}(-\mu, \mu_0, \phi - \phi_0) \\
&\quad + 2\pi \int_0^1 R_{\lambda, 0, x, y}(-\mu, \mu') T_{\lambda, 0}(-\mu_0, -\mu'; \tau_\lambda) d\mu' \\
&\quad + \pi \cos(\phi - \phi_0) \int_0^1 R_{\lambda, 1, x, y}(-\mu, \mu') T_{\lambda, 1}(-\mu_0, -\mu'; \tau_\lambda) d\mu' \\
&\quad + A_{\lambda, x, y}^{hem}(\mu_0; \tau_\lambda) \cdot s_\lambda(\tau_\lambda) \cdot 2 \int_0^1 R_{\lambda, 0, x, y}(-\mu, \mu') \mu' d\mu']
\end{aligned} \tag{24}$$

where $R_{\lambda, x, y}$ within the integrals has also been expanded in a two term cosine series in $\phi - \phi'$,

$$R_{\lambda, x, y}(-\mu, \mu', \phi - \phi') = R_{\lambda, 0, x, y}(-\mu, \mu') + \cos(\phi - \phi') R_{\lambda, 1, x, y}(-\mu, \mu'). \tag{25}$$

After some rearranging (24) can be used in an iterative scheme to determine $R_{\lambda, x, y}$. We have,

$$\begin{aligned}
R_{\lambda, x, y}^{(n+1)}(-\mu, \mu_0, \phi - \phi_0) &= \frac{E_{\lambda, x, y}(\mu_0; \tau_\lambda)}{\mu_0 E_{0, \lambda} e^{-\tau_\lambda / \mu_0}} \cdot r_{\lambda, x, y}(-\mu, \mu_0, \phi - \phi_0; \tau_\lambda) \\
&\quad - \frac{2\pi}{e^{-\tau_\lambda / \mu_0}} \int_0^1 R_{\lambda, 0, model}^{(n)}(-\mu, \mu') T_{\lambda, 0}(-\mu_0, -\mu'; \tau_\lambda) d\mu' \\
&\quad - \frac{\pi \cos(\phi - \phi_0)}{e^{-\tau_\lambda / \mu_0}} \cdot \int_0^1 R_{\lambda, 1, model}^{(n)}(-\mu, \mu') T_{\lambda, 1}(-\mu_0, -\mu'; \tau_\lambda) d\mu' \\
&\quad - \frac{A_{\lambda, x, y}^{hem}(\mu_0; \tau_\lambda) \cdot s_\lambda(\tau_\lambda) \cdot E_{\lambda, x, y}(\mu_0; \tau_\lambda)}{\mu_0 E_{0, \lambda} e^{-\tau_\lambda / \mu_0}} \cdot 2 \int_0^1 R_{\lambda, 0, model}^{(n)}(-\mu, \mu') \mu' d\mu'
\end{aligned} \tag{26}$$

where $R_{\lambda, 0, x, y}^{(n)}$ and $R_{\lambda, 1, x, y}^{(n)}$ are replaced by $R_{\lambda, 0, model}^{(n)}$ and $R_{\lambda, 1, model}^{(n)}$, respectively, which are produced from a parameterized BRF model. This step is necessary because $R_{\lambda, 0, x, y}$ and $R_{\lambda, 1, x, y}$ in the integrals of (24) are dependent on μ' , the direction of incidence of the radiance at the surface, and this dependence is displayed in the MISR data only for the single direction, μ_0 , the cosine of the sun angle of the observations. The parameterized BRF model $R_{\lambda, model}^{(n)}$ is specified by fitting it to $R_{\lambda, x, y}^{(n)}$ at the MISR view angles and determining the best fit parameters. Once the parameters are determined, this procedure then allows $R_{\lambda, 0, model}^{(n)}$ and $R_{\lambda, 1, model}^{(n)}$ to be computed from the

expressions

$$R_{\lambda, 0, model}^{(n)}(-\mu, \mu') = \frac{1}{2\pi} \int_0^{2\pi} R_{\lambda, model}^{(n)}(-\mu, \mu', \phi - \phi') d\phi' \quad (27)$$

$$R_{\lambda, 1, model}^{(n)}(-\mu, \mu') \cos(\phi - \phi_0) = \frac{1}{\pi} \int_0^{2\pi} R_{\lambda, model}^{(n)}(-\mu, \mu', \phi - \phi') \cos(\phi' - \phi_0) d\phi'. \quad (28)$$

The BRF model used is that of Rahman et al. [29], modified to allow a nearly linearizable least squares fitting analysis. This modified model is described by

$$R_{\lambda, model}(-\mu, \mu_0, \phi - \phi_0) = r_{0, \lambda} [\mu \mu_0 (\mu + \mu_0)]^{k_\lambda - 1} \cdot \exp[b_\lambda \cdot p(\Omega)] \cdot h_\lambda(-\mu, \mu_0, \phi - \phi_0) \quad (29)$$

with three free parameters, $r_{0, \lambda}$, k_λ , and b_λ . The function h_λ is a factor to account for the hot spot,

$$h_\lambda(-\mu, \mu_0, \phi - \phi_0) = 1 + \frac{1 - r_{0, \lambda}}{1 + G(-\mu, \mu_0, \phi - \phi_0)} \quad (30)$$

with

$$G(-\mu, \mu_0, \phi - \phi_0) = \left[\frac{1 - \mu^2}{\mu^2} + \frac{1 - \mu_0^2}{\mu_0^2} + 2 \frac{\sqrt{1 - \mu^2}}{\mu} \cdot \frac{\sqrt{1 - \mu_0^2}}{\mu_0} \cdot \cos(\phi - \phi_0) \right]^{\frac{1}{2}}. \quad (31)$$

The function $p(\Omega)$ in (29) is assumed to depend only on the scattering angle Ω , the angle between the directions of the incident and reflected radiances, and is defined to be

$$p(\Omega) = \cos \Omega = -\mu \mu_0 + (1 - \mu^2)^{\frac{1}{2}} \cdot (1 - \mu_0^2)^{\frac{1}{2}} \cdot \cos(\phi - \phi_0) \quad (32)$$

The fitting of $R_{\lambda, model}^{(n)}$ is accomplished by first taking the logarithm of each function, differencing them, and then computing the sum of the squares of the residuals,

$$S = \sum_i [\ln R_{\lambda, x, y}^{(n)}(-\mu_i, \mu_0, \phi_i - \phi_0) - \ln R_{\lambda, model}^{(n)}(-\mu_i, \mu_0, \phi_i - \phi_0)]^2, \quad (33)$$

where the summation is over the cameras used and

$$\begin{aligned} \ln R_{\lambda, model}^{(n)}(-\mu_i, \mu_0, \phi_i - \phi_0) = & \ln r_{0, \lambda}^{(n)} + (k_{\lambda}^{(n)} - 1) \cdot \ln[\mu_i \mu_0 (\mu + \mu_0)] + b_{\lambda}^{(n)} \cdot p(\Omega_i) \\ & + \ln h_{\lambda}^{(n)}(-\mu_i, \mu_0, \phi_i - \phi_0) \end{aligned} \quad (34)$$

The model is given explicit dependence on the iteration count through the superscript (n) because the parameters are updated every time $R_{\lambda, x, y}^{(n)}$ is iterated. Aside from the $\ln h_{\lambda}^{(n)}$ term in (34), we note that $\ln R_{\lambda, model}$ is linear in the three model parameters in $r_{0, \lambda}$, k_{λ} , and b_{λ} . The $\ln h_{\lambda}^{(n)}$ term is easily handled by simply using the value of $r_{0, \lambda}$ from the previous iteration,

$$h_{\lambda}^{(n)}(-\mu, \mu_0, \phi - \phi_0) = 1 + \frac{1 - r_{0, \lambda}^{(n-1)}}{1 + G(-\mu, \mu_0, \phi - \phi_0)}, \quad (35)$$

where $r_{0, \lambda}^{(-1)}$ is set equal to zero. Once the parameters are found, $R_{\lambda, 0, model}^{(n)}$ and $R_{\lambda, 1, model}^{(n)}$ can be computed using (27) and (28).

As a good initial estimate to start the iteration, we set the BRF equal to the HDRF, i.e.,

$$R_{\lambda, x, y}^{(0)}(-\mu, \mu_0, \phi - \phi_0) = r_{\lambda, x, y}(-\mu, \mu_0, \phi - \phi_0; \tau_{\lambda}) \quad (36)$$

The iteration process expressed by (26) is then cycled until convergence is achieved. Convergence is measured by the metric D , defined as

$$D = \frac{1}{A_{\lambda, x, y}^{hem}(\mu_0; \tau_{\lambda})} \cdot \left\{ \sum_i [R_{\lambda, x, y}^{(n+1)}(-\mu_i, \mu_0, \phi_i - \phi_0) - R_{\lambda, x, y}^{(n)}(-\mu_i, \mu_0, \phi_i - \phi_0)]^2 \right\}^{\frac{1}{2}} \quad (37)$$

where the summation is over the cameras used. When $D \leq D_{thresh}$, a threshold value, the iteration process is terminated. Like the HDRF/BHR iteration process, this process is also very stable and efficient in achieving convergence.

Finally, the DHR, $A_{\lambda, x, y}^{dir}$, is determined by directly integrating the BRF from the final iteration, $R_{\lambda, x, y}^{(N)}$, over the hemisphere, assuming the azimuth angle model of (25),

$$\begin{aligned}
A_{\lambda, x, y}^{dir}(\mu_0) &= \frac{1}{\pi} \int_0^1 \int_0^{2\pi} R_{\lambda, x, y}(-\mu, \mu_0, \phi - \phi_0) \mu d\mu d\phi \\
&= 2 \int_0^1 R_{\lambda, 0, x, y}^{(N)}(-\mu, \mu_0) \mu d\mu
\end{aligned} \tag{38}$$

Since $R_{\lambda, x, y}^{(N)}$ is determined only at the MISR camera angles,

$$R_{\lambda, 0, x, y}^{(N)}(-\mu_0) = \frac{R_{\lambda, x, y}^{(N)}(-\mu, \mu_0, \phi_a - \phi_0) \cos(\phi_f - \phi_0) - R_{\lambda, x, y}^{(N)}(-\mu, \mu_0, \phi_f - \phi_0) \cos(\phi_a - \phi_0)}{\cos(\phi_f - \phi_0) - \cos(\phi_a - \phi_0)} \tag{39}$$

where ϕ_f and ϕ_a are the forward and aftward view azimuth angles for each symmetrically viewing camera pair.

VI. PAR-INTEGRATED BHR AND DHR

For radiation balance and climate studies the shortwave (the effective wavelength range of the solar spectrum) BHR is needed, split into the photosynthetically active radiation (PAR) regime (400 -700 nm), and the non-PAR regime (>700 nm). Since MISR has only four narrow bands in the shortwave region of the spectrum, additional information concerning the spectral shape of the surface BHR is needed to transform the four MISR spectral BHR's to a full shortwave BHR. This type of information can be obtained from other EOS instruments, e.g., the Moderate Resolution Imaging Spectroradiometer (MODIS), and we leave the algorithm to retrieve it to the post-launch era. However, since three of the four MISR bands are in the PAR spectral region, we include a PAR-integrated BHR and DHR as part of our at-launch surface product. They are a measure of the amount of incident photosynthetically active radiation absorbed by the complete canopy-soil system and can be compared to FPAR, another MISR surface product parameter [10]. Unlike the surface products described so far, which are calculated for a subregion size of 1.1 km, these PAR-integrated albedos are calculated for the 17.6 km region.

The PAR-integrated BHR, A_{PAR}^{hem} , can be written as

$$A_{PAR}^{hem}(\mu_0; \tau_\lambda) = \frac{\int_{400}^{700} \langle M_\lambda(\mu_0; \tau_\lambda) \rangle d\lambda}{\int_{400}^{700} \langle E_\lambda(\mu_0; \tau_\lambda) \rangle d\lambda}, \quad (40)$$

where

$$\langle M_\lambda(\mu_0; \tau_\lambda) \rangle = \frac{1}{N_{sub_{x,y}}} \sum M_{\lambda, x, y}(\mu_0; \tau_\lambda) \quad (41)$$

$$\langle E_\lambda(\mu_0; \tau_\lambda) \rangle = \frac{1}{N_{sub_{x,y}}} \sum E_{\lambda, x, y}(\mu_0; \tau_\lambda) \quad (42)$$

with the summation taken *over* the N_{sub} subregions within the 17.6 km region. The surface irradiance $E_{\lambda, x, y}$ is calculated from (8) and the radiant exitance $M_{\lambda, x, y}$ is calculated from (7), written as

$$M_{\lambda, x, y}(\mu_0; \tau_\lambda) = A_{\lambda, x, y}^{hem}(\mu_0; \tau_\lambda) \cdot E_{\lambda, x, y}(\mu_0; \tau_\lambda). \quad (43)$$

An identical calculation is done to obtain the PAR-integrated DHR, A_{PAR}^{dir} , but with

$$E_{\lambda, x, y}(\mu_0) = \mu_0 E_{0, \lambda}, \quad (44)$$

$$M_{\lambda, x, y}(\mu_0) A_{\lambda, x, y}^{dir}(\mu_0) = \mu_0 E_{0, \lambda}. \quad (45)$$

The spectral integration in (40), and its counterpart for A_{PAR}^{dir} , is then carried out using a piecewise, linear curve to approximate the spectrum between the 3 MISR wavelengths contained within the integral. This enables the integrals to be replaced by weighted sums of the spectral parameters, with the weights being pre-established. Details of this procedure can be found in [25].

VII. SURFACE RADIATION PARAMETERS

The spectral HDRF and BHR and the spectral BRF and DHR, retrieved by means of the algorithms described in Sections IV and V, are archived as part of the MISR standard surface product. Additional parameters, not explicitly archived but which can be easily calculated from the

standard aerosol and surface parameters, include:

1) the surface spectral irradiance $E_{\lambda, x, y}$ (incident radiant flux density or flux) for the ambient atmosphere, given by (8), and for no atmosphere, given by (44);

2) the surface spectral radiant exitance, $M_{\lambda, x, y}$, (exiting radiant flux density or flux) for the ambient atmosphere, given by (43), and for no atmosphere, given by (45);

3) the surface-leaving spectral radiance, $L_{\lambda, x, y}^{surf}$, for the ambient atmosphere,

$$L_{\lambda, x, y}^{surf}(-\mu, \mu_0, \phi - \phi_0; \tau_\lambda) = \frac{1}{\pi} \cdot r_{\lambda, x, y}(-\mu, \mu_0, \phi - \phi_0; \tau_\lambda) E_{\lambda, x, y}(\mu_0; \tau_\lambda), \quad (46)$$

where (4) and (5) were used, and for no atmosphere,

$$L_{\lambda, x, y}^{surf}(-\mu, \mu_0, \phi - \phi_0; \tau_\lambda) = \frac{1}{\pi} \cdot R_{\lambda, x, y}(-\mu, \mu_0, \phi - \phi_0) \mu_0 E_{0, \lambda}, \quad (47)$$

where (2) and (22) were used.

VIII. SURFACE CHARACTERIZATION PARAMETERS

The surface products discussed so far are very basic and are retrieved using straightforward techniques, rooted in well developed 1-dimensional radiative transfer theory of the atmosphere/surface boundary problem. The advanced MISR surface products, which include a biome-based surface description or classification, leaf area index (LAI), and FPAR, require a more sophisticated approach to their retrieval. The algorithm used to determine these three products uses as input the retrieved spectral BHR and BRF/DHR products, described in Sections IV and V. Fundamental to the operation of the algorithm is the use of precomputed radiation parameters, which are derived from 3-dimensional modeling of complex vegetation canopies and their underlying surface (e.g., [30]) and stored in a lookup table labelled the Canopy Architecture Radiative Transfer (CART) file [25]. These precomputed parameters allow a fast and accurate computation of BHR and BRF/DHR values at the top of the canopy for a wide variety of canopy/soil models, in which biome type, LAI, and soil reflectance can vary.

The algorithm does a comparison of the retrieved and modeled reflectances and reflectance

factors, using a two step procedure. First, the retrieved BHR and DHR in the four MISR spectral bands are compared to the corresponding modeled values, which are a function of biome type, LAI, and soil reflectance. Only for those models which pass this test is a second comparison test performed between the retrieved spectral BRF values and the modeled values. The canopy/soil models which pass this second test are considered to be successful representations of the actual canopy/soil condition. A weighted average LAI and its spread are calculated for each biome type of the successful models. The biome type with the minimum spread in LAI is then used to calculate FPAR. The algorithm considers six distinct biome types for the models - grasses and cereal crops, semi-arid shrublands, broadleaf crops, savanna, broadleaf forest, and needle leaf forest. Two additional and non-vegetative surface classifications include the categories water and barren. Land sub-regions are classified as barren when the NDVI is less than a threshold value and, consequently, LAI and FPAR both set to zero. Additional information and details about this algorithm can be found in [10], [25].

By introducing more realism into the modeling of the canopy architecture and subsequent radiative transfer process, this algorithm represents a significant advancement in the effort to retrieve canopy biophysical parameters. One current method to determine FPAR, for example, is based on a biome-dependent, simple linear relationship between FPAR and the vegetation index [31], [32], which ignores much of the variation in canopy architecture and soil reflectance inherent in real canopies. We view the physically-based MISR LAI/FPAR algorithm as a first step toward future algorithms which will be designed to retrieve a larger list of canopy biophysical products.

IX. SURFACE RETRIEVAL SIMULATIONS

The accuracy of the HDRF/BHR and BRF/DHR retrieval algorithms was studied by applying them to simulated MISR radiance data. These radiances were computed using a number of different, directionally reflecting, surface types, overlain by an atmosphere containing aerosols. The bidirectional reflectance factors describing the model surface reflection properties were derived from measurements of 11 distinct types of natural surfaces in the two AVHRR wavelength bands 1 (0.58-0.67 μm) and 2 (0.73- 1.1 μm) [33] -[35]. These measurements are especially useful in modeling work because of the fairly complete angular coverage in both the view and Sun directions. It should be noted that the reported measurements are actually HDRF's, i.e., no correction was made for atmospheric effects, but in our study we treated the measurements as

BRF's when modeling the TOA radiances. This approximation is not significant since we are primarily interested in the variety of angular shapes and reflectance values that the measurements offer. We also assumed that the AVHRR bands 1 and 2 were equivalent to the MISR red and near IR bands at 672 and 866 nm, respectively, for each of the derived BRF models. The 11 surface types are listed in Table 1 along with their BHR at 672 nm.

The atmospheric model used for the simulated MISR radiance calculations contains both Rayleigh and aerosol scattering. The selected aerosol was a sulfate/nitrate type at 70% relative humidity (RH) with an effective particle radius of 0.21 μm and with a phase function described by an asymmetry parameter of 0.68 and a single-scattering albedo of 1.0 at a wavelength of 672 nm. The aerosol was distributed in the atmosphere with a particle density scale height of 2 km. A number of aerosol turbidity conditions were investigated, ranging from a light aerosol load (optical depth of 0.1 at 672 nm) to a relatively heavy load (optical depth of 0.4). The simulated data were calculated for three solar zenith angles ($\theta_0 = 25^\circ, 45^\circ, \text{ and } 65^\circ$) and three MISR azimuth angle differences ($\Delta\phi = 30^\circ, 60^\circ, \text{ and } 90^\circ$) as measured from the principal plane. The radiative transfer calculations were done using a multiple scattering, matrix-operator technique [36] which included all the interactions between the surface and the atmosphere.

Three different scenarios were studied to test the sensitivity of the HDRF retrieval to atmospheric conditions. The first was the use of the correct aerosol type and column amount in the retrieval process to gauge how well the algorithm works under optimum conditions. Next, the correct aerosol type was used but the column amount was decreased a bit from the true value. Finally, the correct aerosol column amount was used but the aerosol type was modified by increasing the RH from 70 to 99%, thus increasing the particle effective radius to 0.64 μm . To gauge the performance of the HDRF/BHR retrieval algorithm, we define a metric $\delta_{\lambda, x, y}$, the average HDRF deviation, as

$$\delta_{\lambda, x, y}(\tau_\lambda) = \frac{1}{9} \cdot \sum_i \left| r_{\lambda, x, y}(-\mu_i, \mu_0, \phi_i - \phi_0; \tau_\lambda) - r_{\lambda, x, y}^{true}(-\mu_i, \mu_0, \phi_i - \phi_0; \tau_\lambda) \right|, \quad (48)$$

where $r_{\lambda, x, y}$ and $r_{\lambda, x, y}^{true}$ are the retrieved and true HDRF, respectively. and the summation is over the nine MISR camera angles. Figure 1 shows the HDRF retrieval results of the 11 surface cases at 672 nm for $\theta_0 = 45^\circ$ and all three $\Delta\phi$, using the correct aerosol type (sulfate/nitrate at RH 70%) and column amount (optical depth of 0.4). It is apparent from this figure that the retrieval accuracy is approximately proportional to the reflectance level of the surface. This is clearly demonstrated

by [he relatively large average deviations of the first four cases compared to the others and the similar pattern exhibited by the BHR listed in Table 1. Also apparent is the fact that the retrieval accuracy does not depend strongly on $\Delta\phi$, the azimuth angle difference between the plane of the measurements and the principal plane, although there is a tendency towards less accurate retrievals when $\Delta\phi$ is near 90° . In general the average deviation is about 2% of the BHR value, indicating the high intrinsic accuracy of the HDRF/BHR retrieval algorithm under optimum conditions. Similar results were found for the retrievals at the other two solar zenith angles, $\theta_0 = 25^\circ$ and 65° . The BHR retrieval results corresponding to the HDRF results of Figure 1 are shown in Figure 2. Here, the metric used to describe the BHR retrieval accuracy is the BHR error, $\epsilon_{\lambda, x, y}$, defined as

$$\epsilon_{\lambda, x, y}(\tau_\lambda) = A_{\lambda, x, y}^{hem}(\mu_0; \tau_\lambda) - A_{\lambda, x, y}^{hem, true}(\mu_0; \tau_\lambda) \quad (49)$$

where $A_{\lambda, x, y}^{hem}$ and $A_{\lambda, x, y}^{hem, true}$ are the retrieved and true values, respectively. Comparison of Figures 1 and 2 shows that the BHR error is typically somewhat larger than the average HDRF deviation, indicative of the fact that the BHR integration over the upward directed hemisphere includes large amounts of solid angle where no measurements are obtained. However, the overall uncertainty in the retrieved BHR is generally less than 5% for all the solar and viewing geometries considered in this study.

Figures 3 and 4 show the HDRF and BRF retrieval at 672 nm as a function of the MISR camera view zenith angles for surface case 1 (soil), an aerosol optical depth of 0.4, $\Delta\phi = 30^\circ$, and solar zenith angles, $\theta_0 = 45^\circ$ and 65° , respectively. The HDRF and BRF retrieval for surface case 7 (pine forest) under the same atmospheric and Sun-view conditions are shown in Figures 5 and 6. The difference between the HDRF and BRF generally increases with increasing optical depth: Figures 3-6 show that this difference also increases with increasing solar zenith angle. The BRF retrieval is noticeably less accurate than the HDRF retrieval but, nevertheless, produces a very acceptable result.

All results presented up to now were obtained using the correct aerosol type and amount. However, a certain amount of error or uncertainty is inevitable when an aerosol retrieval is performed using the MISR data [22]. For optical depths less than 0.5, the expected optical depth uncertainty will be about 0.05 with a possibility for misidentification of aerosol type. To determine the impact of these types of errors on the accuracy of the surface retrievals, the properties of the

aerosol model used in the retrievals were allowed to deviate from those of the correct model. First, we modified the aerosol column amount, using an optical depth of 0.35 instead of the correct value of 0.4 in the surface retrieval algorithm. The HDRF retrieval results, shown in Figure 7 and the BHR results, shown in Figure 8, for $\theta_0 = 45^\circ$ should be compared to those in Figures 1 and 2. We note that the average HDRF deviation in Figure 7 is about 0.01 for each surface case. This is approximately 2.5 times larger than the average deviations in Figure 1 for the first four cases and approximately 10 times larger for the remaining cases which have a much smaller BHR. Also, the BHR errors in Figure 8 are now positively biased by more than 0.01 compared to those in Figure 2, a result of using too small an optical depth.

Another example of the consequences of using an inaccurate aerosol model is the case where the correct optical depth is used but with a modified aerosol type (sulfate/nitrate at RH 99% instead of 70%). The results of the HDRF and BHR retrieval for this case are displayed in Figures 9 and 10, respectively. Again, the results are biased by amounts which are much larger than the inherent accuracy of the HDRF/BHR retrieval process, as illustrated in Figures 1 and 2. Clearly, it is the accuracy of the aerosol retrieval process that will be the limiting factor in determining the degree of uncertainty in many of the surface products.

The results presented in Figures 1-10 are for an aerosol amount described by an optical depth of 0.4 at 672 nm. Retrievals on simulated data with smaller optical depths show correspondingly smaller errors. However, the projected 0.05 uncertainty in optical depth for MISR aerosol retrievals, even when the optical depth is small, will produce biases in the HDRF and BHR retrievals which are comparable to those observed in Figures 7 and 8. Expressions for the formal uncertainties of the retrieved HDRF and BHR, which include the effects of uncertainties in the aerosol properties, can be found in [25]. These uncertainty estimates will be archived as part of the MISR standard data products.

X. DISCUSSION

The retrieval techniques described in Sections IV, V, and VIII form the core of the MISR surface product algorithms. They take full advantage of the multi-angle nature of the MISR datasets, allowing a more accurate determination of the surface directional reflectance properties than can be obtained with conventional, single-view instruments. For example, if the surface leav-

ing radiance, $L_{\lambda, x, y}^{surf}$, is to be retrieved from single-view data, then it would be computed using (11), an expression based on the assumption of a lambertian surface. This expression, however, is only approximate and describes just the initial estimate of $L_{\lambda, x, y}^{J_{surf}}$ in the iteration procedure used by the MISR multiangle HDRF/BHR retrieval algorithm. This algorithm and the BRF/DHR algorithm are designed to accommodate MISR data without a full complement of nine view angles, due to possible cloud contamination or instrument problems in one or more cameras. Quality assessment parameters, which include information on the number of camera views used in the retrieval process, are archived to help assess the accuracy of the surface products.

Once the spectral HDRF and BHR are retrieved for a land subregion, they are then used as inputs to additional algorithms to retrieve the BRF and DHR, the PAR-integrated BHR and DHR, and the surface classification, the LAI, and the FPAR. When the surface retrieval is done for ocean samples, however, only the spectral HDRF is determined. For ocean, the surface-leaving radiance can be expressed as,

$$L_{\lambda, x, y}^{surf}(-\mu, \mu_0, \phi - \phi_0; \tau_\lambda) = L_{\lambda, x, y}^{water}(-\mu, \mu_0, \phi - \phi_0; \tau_\lambda) + L_{\lambda, x, y}^{glitter}(-\mu, \mu_0, \phi - \phi_0; \tau_\lambda) \quad (50)$$

where $L_{\lambda, x, y}^{water}$ is the water-leaving radiance, which is that part of the radiance incident on the surface which penetrates the surface, scatters within the water proper, and then exits the surface, and $L_{\lambda, x, y}^{glitter}$ is the radiance reflected directly from the surface (Fresnel scattering) [37] and a contribution due to whitecaps [38]. When the aerosol retrieval is performed, the component of the TOA radiance due to $L_{\lambda, x, y}^{glitter}$,

$$L_{\lambda, x, y}^{TOA, glitter}(-\mu, \mu_0, \phi - \phi_0; \tau_\lambda) = e^{-\tau_\lambda/\mu} \cdot L_{\lambda, x, y}^{glitter}(-\mu, \mu_0, \phi - \phi_0; \tau_\lambda) + \int_0^{12\pi} \int_0^{2\pi} T_\lambda(-\mu, -\mu', \phi - \phi'; \tau_\lambda) L_{\lambda, x, y}^{glitter}(-\mu', \mu_0, \phi' - \phi_0; \tau_\lambda) d\mu' d\phi' \quad (51)$$

is also determined, based on precomputed values contained in the SMART dataset. Therefore, the iteration procedure of the HDRF algorithm, expressed by (14), becomes an algorithm for retrieving $L_{\lambda, x, y}^{water}$ instead of $L_{\lambda, x, y}^{surf}$ by setting L_{λ}^{atm} in the expression equal to the sum of L_{λ}^{atm} and $L_{\lambda, x, y}^{TOA, glitter}$. Although $L_{\lambda, x, y}^{water}$ is retrieved for all nine MISR view angles, only the most glitter-free of the two radiances at 45.6° zenith angle will be archived. Also, these radiances will be retrieved

only for the two spectral bands at 446 and 558 nm; $L_{\lambda, x, y}^{water}$ for the other two spectral bands are assumed to be zero. These two single-view radiances are then used to determine the phytoplankton pigment concentration, based on an algorithm developed for the Coastal Zone Color Scanner [39]. There are alternative, more conventional, ways of determining $L_{\lambda, x, y}^{water}$, based on single-view satellite data. In particular, this product is currently being produced from SeaWiFS data using an algorithm [12] which is a prototype for the one under development for MODIS [11], an instrument on the same platform as MISR. A modified Version of this algorithm will be used with MISR data, in addition to the HDRF algorithm, so that the two sets of results can be compared.

Validation of the MISR surface products will rely on several sources of data including **radiometrically** calibrated aircraft observations, together with field observations of downwelling diffuse sky spectral radiance and **irradiance**, the direct solar spectral **irradiance**, and surface spectral **HDRF**. Details on planned field campaigns, experimental methodologies, and instrument calibration and data reduction procedures are documented in [40] and [41]. As the surface retrieval simulations have demonstrated, the accuracy of the MISR surface products (and the surface products from other spacecraft instruments) depends heavily on how well the aerosol properties are known. This requirement on accuracy also applies to the surface radiation parameters, described in Section VII, which can be derived from the MISR products. Thus, the validation plan is structured around the requirement of obtaining measurement sets from which aerosol and surface properties can be determined together.

XI. CONCLUDING REMARKS

By monitoring the global environment via multi-angle, spectral imagery, MISR will make unique contributions to Earth System Science research. It will produce a number of surface data products (see Table 2) on a daily basis which will be of interest to people in research disciplines covering broad areas of land, ocean and atmospheric science. Using atmospheric information archived during the aerosol retrieval process, surface radiometric quantities, e.g., the spectral radiances and radiant flux densities, can also be determined from these surface products. We anticipate other progressions to new and more advanced products, through ingestion of non-MISR data and the development of improved algorithms.

ACKNOWLEDGMENT

We are grateful to Brian **Rheingans** for his assistance with the graphical work. This research was carried out by the Jet Propulsion Laboratory, California Institute of Technology, under contract with the National Aeronautics and Space Administration.

REFERENCES

- [1] R.E. Dickinson, "Land surface processes and climate-surface albedos and energy balance," *Adv. Geophys*, vol. 25, pp. 305-353, 1981.
- [2] D.S. Kimes, P. J. Sellers and D. J. Diner, "Extraction of spectral hemispherical reflectance (albedo) of surfaces from nadir and directional reflectance data," *Int. J. Remote Sensing*, vol.8, pp. 1727-1746, 1987.
- [3] P.J. Sellers, "Canopy reflectance, photosynthesis and transpiration," *Int. J. Remote Sensing*, vol. 8, pp. 1335-1372, 1985.
- [4] P.J. Sellers, "Canopy reflectance, photosynthesis and transpiration II: The role of biophysics in the linearity of their interdependence," *Remote Sensing Environment*, vol. 21, pp. 143-183, 1987.
- [5] J. Charney, W.J. Quirk, S. Chow, and J. Kornfield, "A comparative study of the effects of albedo change on droughts in semi-arid regions," *J. Atmos. Sci.*, vol. 34, pp. 1366-1385, 1977.
- [6] R.E. Dickinson, B. Pin(y, and M. M. Verstraete, "Relating surface albedos in GCM to remotely sensed data," *Agricultural and Forest Meteorology*, vol. 52, pp. 109-131, 1990.
- [7] Y. Mintz, *The Global Climate*, J.T. Houghton, cd., Cambridge University Press, Cambridge, 1984.
- [8] N. Gobron, B. Pinty, M.M. Verstraete, R.B. Myneni, J.V. Martonchik, Yu. Knyazikhin, and D.J. Diner, "The potential of multi-angular spectral measurements to characterize land surfaces: Conceptual approach and exploratory application," *IEEE Trans. Geosci. and Remote Sensing*, (this issue), 1998.
- [9] D.J. Diner, J.C. Beckert, T.H. Reilly, C.J. Bruegge, J.E. Cone], R.A. Kahn, J.V. Martonchik, T.P. Ackerman, R. Davies, S.A.W. Gerstl, H.R. Gordon, J.-P. Muller, R.B. Myneni, P. Sellers, B. Pinty, and M.M. Verstraete, "Multi-angle Imaging SpectroRadiometer instrument description and experiment overview," *IEEE Trans. Geosci. and Remote Sensing*, (this issue), 1998.
- [10] Yu. Knyazikhin, R. Myneni, J. Martonchik, D. Diner, B. Pinty, and M. Verstraete, "Estimation of vegetation canopy leaf area index and fraction of absorbed photosynthetically active radiation from atmosphere-corrected MISR data," *J. Geophys. Res.* (in preparation).
- [11] H.R. Gordon, *MODIS Normalized Water-leaving Radiance Algorithm Theoretical Basis Document*, Version 2, Submitted Nov. 1, 1994 under NASA/GSFC Contract NAS5-31363,

1994.

[12] H.R. Gordon and M. Wang, "Retrieval of water-leaving radiance and aerosol optical thickness over the oceans with SeaWiFS: A preliminary algorithm," *Appl. Opt.*, vol. 33, pp. 443-452, 1994.

[13] S. Chandrasekhar, *Radiative Transfer*. Dover Publications, Inc., New York, 1960.

[14] F. Cavayas, "Modelling and correction of topographic effect using multi-temporal satellite images," *Canadian J. Remote Sensing*, vol. 13, pp. 49-67, 1987.

[15] P.M. Teillet, B. Guindon, and D.G. Goodenough, "On the slope-aspect correction of multispectral scanner data," *Canadian J. Remote Sensing*, vol. 8, pp. 84-106, 1982.

[16] R.J. Woodham, and T.K. Lee, "Photometric method for radiometric correction of multispectral scanner data," *Canadian J. Remote Sensing*, vol. 11, pp. 132-161, 1985.

[17] M.H. Gray, "Radiometric correction of satellite imagery for topographic and atmospheric effects," M. Sc. Thesis, Faculty of Forestry, University of British Columbia, Vancouver, BC., 1986.

[18] D.J. Diner, D.J. and J. V. Martonchik, "Influence of aerosol scattering on atmospheric blurring of surface features," *IEEE Trans. Geosci. Remote Sensing*, vol. GE-23, pp. 618-624, 1985.

[19] D.J. Diner and J.V. Martonchik, "Atmospheric transfer of radiation above an inhomogeneous non-lambertian reflective ground. I. Theory," *J. Quant. Spectrosc. Radiat. Trans.*, vol.31, pp. 97-125, 1984.

[20] D.J. Diner and J.V. Martonchik, "Atmospheric transfer of radiation above an inhomogeneous non-lambertian reflective ground. II. Computational considerations and results," *J. Quant. Spectrosc. Radiat. Trans.*, vol.32, pp. 279-304, 1984

[21] D.J. Diner, J.V. Martonchik, E.D. Danielson, and C.J. Bruegge, "Atmospheric correction of high resolution land surface images," *Proceedings of the IGARSS '89 Symposium*, (Vancouver, Canada), 1989.

[22] J.V. Martonchik, D.J. Diner, R.A. Kahn, T.P. Ackerman, M.M. Verstraete, B. Pinty, and H.R. Gordon, "Techniques for the retrieval of aerosol properties over land and ocean using multi-angle imaging," *IEEE Trans. Geosci. Remote Sensing*, (this issue).

[23] D.J. Diner, W.A. Abdou, H.R. Gordon, R.A. Kahn, Y. Knjazikhin, J.V. Martonchik, S.

McMuldroy, R. Myneni, R.A. West, *Level 2 Ancillary Products and Datasets Algorithm Theoretical Basis*, JPL D- 13402, Rev. A., 1997.

[24] P.J. Starks, J.M. Norman, B.L. Blad, E.A. Walter-shea, and C. I. Walthal, "Estimation of shortwave hemispherical reflectance (albedo) from bidirectionally reflected radiance data," *Remote Sensing Environment*, vol. 38, pp. 123-134, 1991.

[25] D.J. Diner, J.V. Martonchik, C. Borel, S.A.W. Gerstl, H.R. Gordon, Y. Knjazikhin, R. Myneni, B. Pinty, and M.M. Verstraete, *Level 2 Surface Retrieval Algorithm Theoretical Basis*, JPL D-401, Rev. C, 1997.

[26] M.M. Verstraete, B. Pinty, and R.E. Dickinson, "A physical model of the bidirectional reflectance of vegetation canopies 1. Theory," *J. Geophys. Res.*, vol. 95, pp. 11,755-11,765, 1990.

[27] Ahmad, S.P. and D.W. Deering (1992). A simple analytical function for bidirectional reflectance. *J. Geophys. Res.* 97, 18,867-18,886.

[28] G. Schluessel, R.E. Dickinson, J.L. Privette, W.J. Emery, and R. Kokaly, "Modeling the bidirectional reflectance distribution function of mixed finite plant canopies and soil," *J. Geophys. Res.*, vol. 99, pp. 10,577-10,600, 1994.

[29] H. Rahman, B. Pinty, and M.M. Verstraete, "Coupled surface-atmosphere reflectance (CSAR) model 2. Semiempirical surface model usable with NOAA Advanced Very High Resolution Radiometer data," *J. Geophys. Res.*, vol. 98, pp. 20,791-20,801, 1993.

[30] R.B. Myneni, G. Asrar, and F.G. Hall, "A three dimensional radiative transfer method for optical remote sensing of vegetated land surfaces," *Remote Sensing Environment*, vol. 41, pp. 105-121, 1992.

[31] R.B. Myneni and D.L. Williams, "On the relationship between FAPAR and NDVI," *Remote Sensing Environment*, vol. 49, pp. 200-211, 1994.

[32] R.B. Myneni, F.G. Hall, P.J. Sellers, and A.L. Marshak, "The interpretation of spectral vegetation indices," *IEEE Trans. Geosci. Remote Sensing*, vol. 33, 481-486, 1995.

[33] D.S. Kimes, "Dynamics of directional reflectance factor distributions for vegetation canopies," *Appl. Opt.*, vol. 22, pp. 1364-1372, 1983.

[34] D.S. Kimes, W.W. Newcomb, R.F. Nelson, and J.B. Schutt, "Directional reflectance distributions of a hardwood and pine forest canopy," *IEEE Trans. Geosci. Remote Sensing*, vol. GE-2-I, pp. 281-293, 1985.

- [35] D.S. Kimes, W.W. Newcomb, C.J. Tucker, I. Zonneveld, W. van Wijngaarden, J. de Leeuw, and G. Epema, "Directional reflectance factor distributions for cover types of Northern Africa in NOAA 7/8 AVHRR Bands 1 and 2," *Remote Sensing Environment*, vol. 18, pp. 1-19, 1985.
- [36] I.P. Grant and G.E. Hunt, "Solution of radiative transfer problems using the invariant S_n method," *Mon. Not. Roy. Astron. Soc.*, vol. 141, pp. 27-41, 1968.
- [37] M.I. Mishchenko and L.D. Travis, "Light scattering by polydisperse, rotationally symmetric nonspherical particles: Linear polarization," *J. Quant. Spectrosc. Radiat. Transfer*, vol. 51, pp. 759-778, 1994.
- [38] P. Koepke, "Effective reflectance of oceanic whitecaps," *Appl. Opt.*, vol. 23, pp. 1816-1824, 1984.
- [39] H.R. Gordon, D.K. Clark, J.W. Brown, O.B. Brown, R.H. Evans, and W.W. Broenkow, "Phytoplankton pigment concentrations in the Middle Atlantic Bight: comparison between ship determinations and Coastal Zone Color Scanner estimates," *Appl. Opt.*, vol. 22, pp. 20-36, 1983.
- [40] J.E. Conel and S. Pilorz, *Science Data Validation Algorithm Theoretical Basis*, JPL D-13403, 1997.
- [41] J.E. Conel and W.C. Ledeboer, *Science Data Validation Plan*, JPL D-12626, 1997.

FIGURE CAPTIONS

Figure 1. Accuracy of HDRF's retrieved from simulated MISR data for 11 surface cases and 3 viewing geometries (azimuth angle from the principal plane, $\Delta\phi = 30^\circ$, 60° , and 90° , all at solar zenith angle, $\theta_0 = 450$). The correct aerosol properties were used in the retrieval process (type is sulfate/nitrate at RH 70% with an optical depth of 0.4).

Figure 2. Accuracy of BHR's retrieved from simulated MISR data for 11 surface cases and 3 viewing geometries (azimuth angle from the principal plane, $\Delta\phi = 30^\circ$, 60° , and 90° , all at solar zenith angle, $\theta_0 = 450$). The correct aerosol properties were used in the retrieval process (type is sulfate/nitrate at RH 70% with an optical depth of 0.4).

Figure 3. Correct and retrieved soil (case 1) reflectance factors versus MISR view zenith angle. The solar zenith angle, $\theta_0 = 45^\circ$ and the azimuth angle from the principal plane, $\Delta\phi = 30^\circ$. The correct aerosol properties were used in the retrieval process (type is sulfate/nitrate at RH 70% with an optical depth of 0.4).

Figure 4. Same as Figure 3, except the solar zenith angle, $\theta_0 = 65^\circ$.

Figure 5. Correct and retrieved pine forest (case 7) reflectance factors versus MISR view zenith angle. The solar zenith angle, $\theta_0 = 45^\circ$ and the azimuth angle from the principal plane, $\Delta\phi = 30^\circ$. correct aerosol properties were used in the retrieval process (type is sulfate/nitrate at RH 70% with an optical depth of 0.4).

Figure 6. Same as Figure 5, except the solar zenith angle, $\theta_0 = 65^\circ$.

Figure 7. Accuracy of HDRF's retrieved from simulated MISR data for 11 surface cases and 3 viewing geometries (azimuth angle from the principal plane, $\Delta\phi = 30^\circ$, 60° , and 90° , all at solar zenith angle, $\theta_0 = 450$). The correct aerosol type (sulfate/nitrate at RH 70%) and an incorrect optical depth of 0.35 were used in the retrieval process.

Figure 8. Accuracy of BHR's retrieved from simulated MISR data for 11 surface cases and 3 viewing geometries (azimuth angle from the principal plane. $\Delta\phi = 30^\circ$, 60° , and 90° , all at solar zenith angle, $\theta_0 = 450$). The correct aerosol type (sulfate/nitrate at RH 70%) and an incorrect

optical depth of 0.35 were used in the retrieval process.

Figure 9. Accuracy of HDRF's retrieved from simulated MISR data for 11 surface cases and 3 viewing geometries (azimuth angle from the principal plane, $\Delta\phi = 30^\circ, 60^\circ$, and 90° , all at solar zenith angle, $\theta_0 = 450$). An incorrect aerosol type (sulfate/nitrate at RH 99%) and the correct optical depth of 0.4 were used in the retrieval process.

Figure 10. Accuracy of BHR's retrieved from simulated MISR data for 11 surface cases and 3 viewing geometries (azimuth angle from the principal **plane**, $\Delta\phi = 30^\circ, 60^\circ$, and 90° , all at solar zenith angle, $\theta_0 = 450$). An incorrect aerosol type (sulfate/nitrate at RH 99%) and the correct optical depth of 0.4 were used in the retrieval process.

Table 1: Surface Models

Case	Surface Type	BRF (672 nm)
1	Soil	0.186
2	Grassland	0.318
3	Steppe Grass	0.211
4	Hard Wheat	0.228
5	Irrigated Wheat	0.063
6	Hardwood Forest	0.035
7	Pine Forest	0.038
8	Lawn Grass	0.058
9	corn	0.082
10	Soybean	0.034
11	Orchard Grass	0.077

Table 2. Summary of MISR Surface Products

Product name	Horizontal sampling (Coverage)	Comments
Hemispherical- Directional Reflectance Factor (HDRF)	1.1 km (Land)	<ul style="list-style-type: none"> • Surface radiance ratioed to that from ideal lambertian reflector at surface • Ambient sky conditions, i.e., direct plus diffuse illumination • 9 viewing angles, 4 spectral bands
Bihemispherical Reflectance (BHR)	1.1 km spectral, 17.6 km PAR (Land)	<ul style="list-style-type: none"> • Radiant exitance ratioed to irradiance at surface (i.e. albedo) • Ambient sky conditions, i.e., direct plus diffuse illumination • 4 spectral bands and PAR integrated
Bidirectional Reflectance Factor (BRF)	1.1 km (Land)	<ul style="list-style-type: none"> • Surface radiance ratioed to that from ideal lambertian reflector at surface • Direct illumination only (no atmosphere) • 9 viewing angles, 4 spectral bands
BRF Model Parameters	1.1 km (Land)	• Model parameters from a fit to the surface BRF
Directional-Hemispherical Reflectance (DHR)	1.1 km spectral, 17.6 km PAR (Land)	<ul style="list-style-type: none"> • Radiant exitance ratioed to irradiance at surface (albedo) • Direct illumination only • 4 spectral bands and PAR-integrated
Surface classification	1.1 km (Land)	<ul style="list-style-type: none"> • Selected from six major biome types plus two non-vegetated types • Determined using physically-based algorithm
NDVI	1.1 km (Land)	• Computed from retrieved spectral DHR
Leaf area index (LAI)	1.1 km (Land)	• Determined using physically-based algorithm
Fractional Absorbed Photosynthetically Active Radiation (FPAR)	17.6 km (Land)	• Determined using physically-based algorithm
Water-leaving radiances	1.1 km (Tropical Ocean)	<ul style="list-style-type: none"> • Most glint-free B-camera viewing angle, blue and green spectral bands, low latitudes, using HDRF and conventional algorithms
Phytoplankton Pigment Concentration	1.1 km (Tropical Ocean)	• Calculated from water-leaving radiances

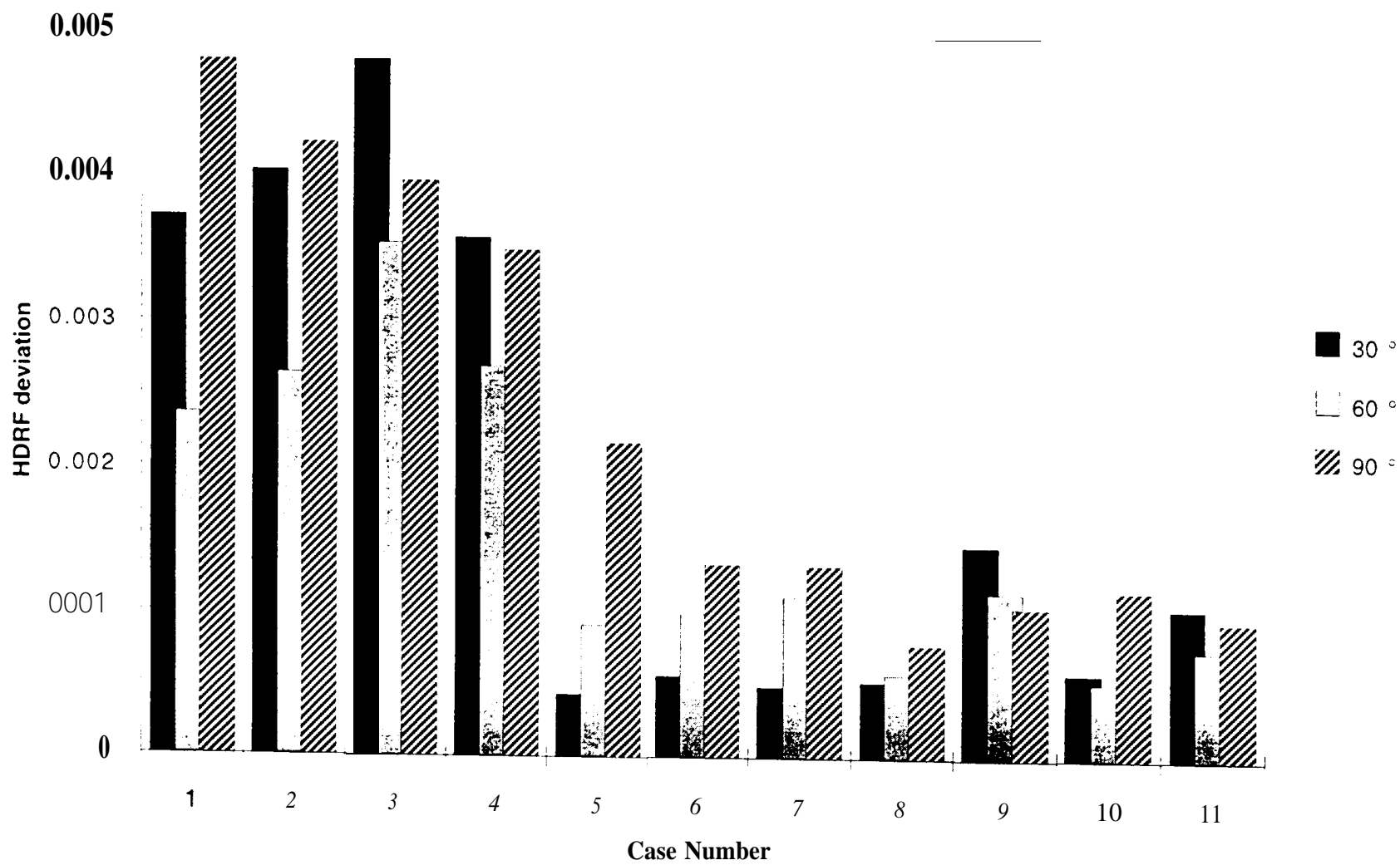
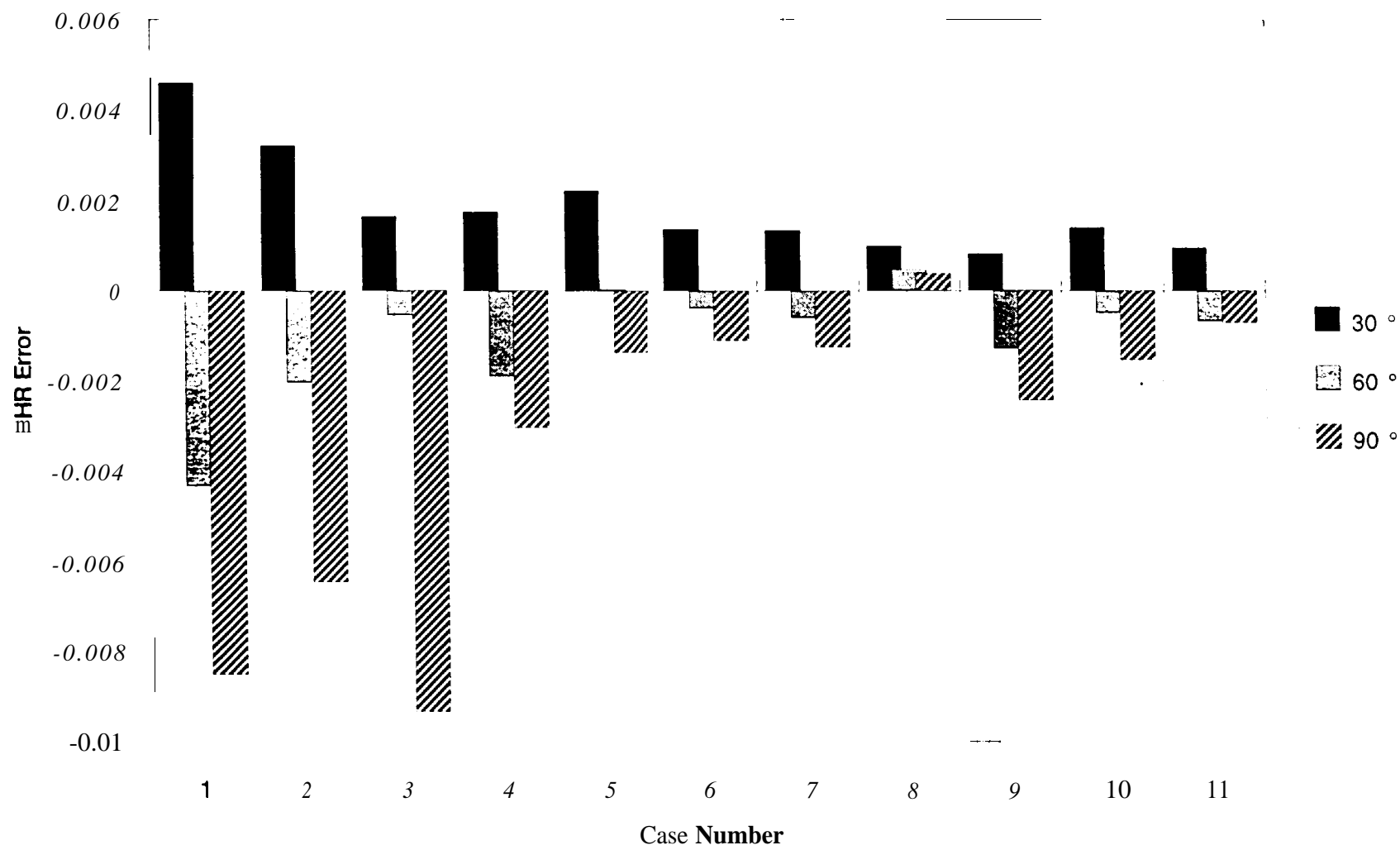
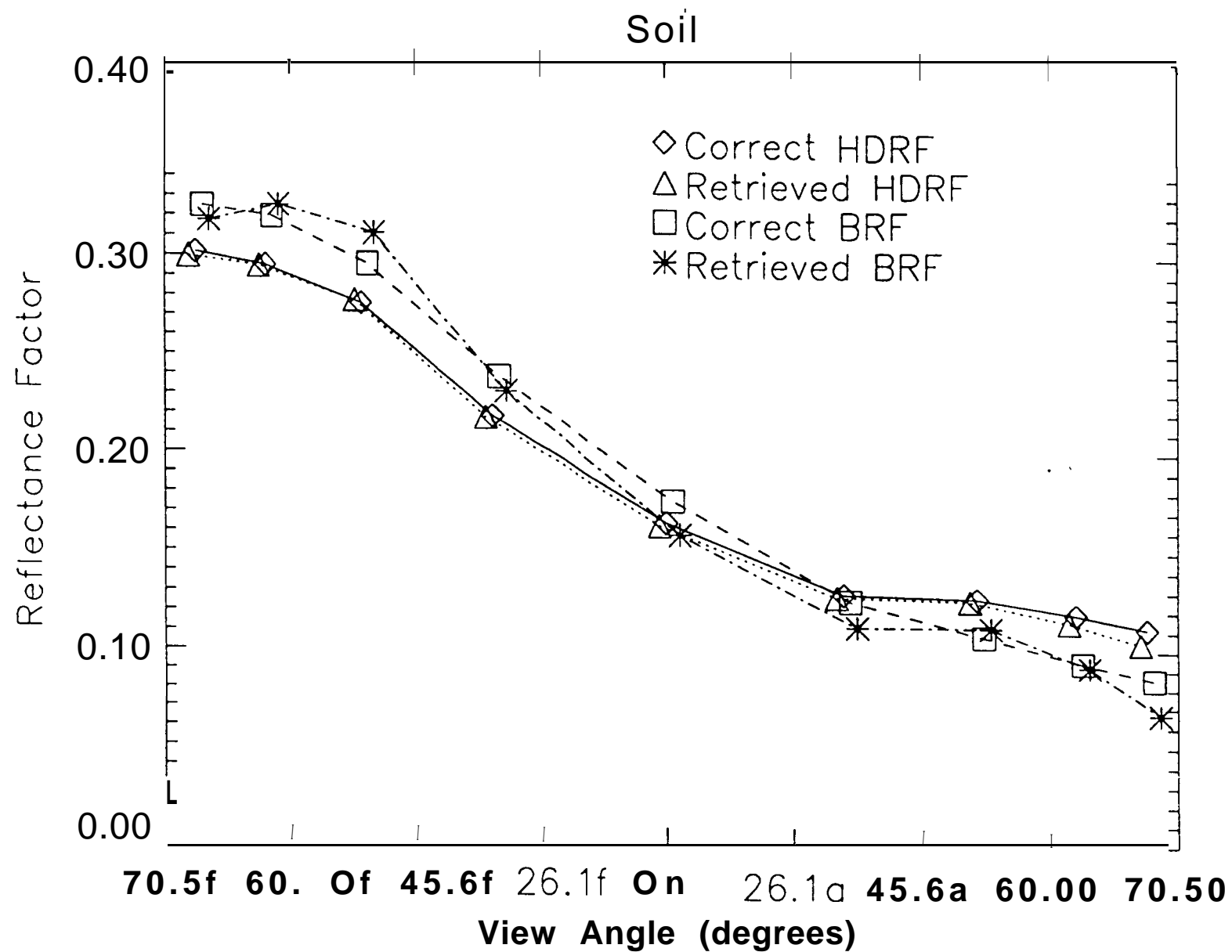
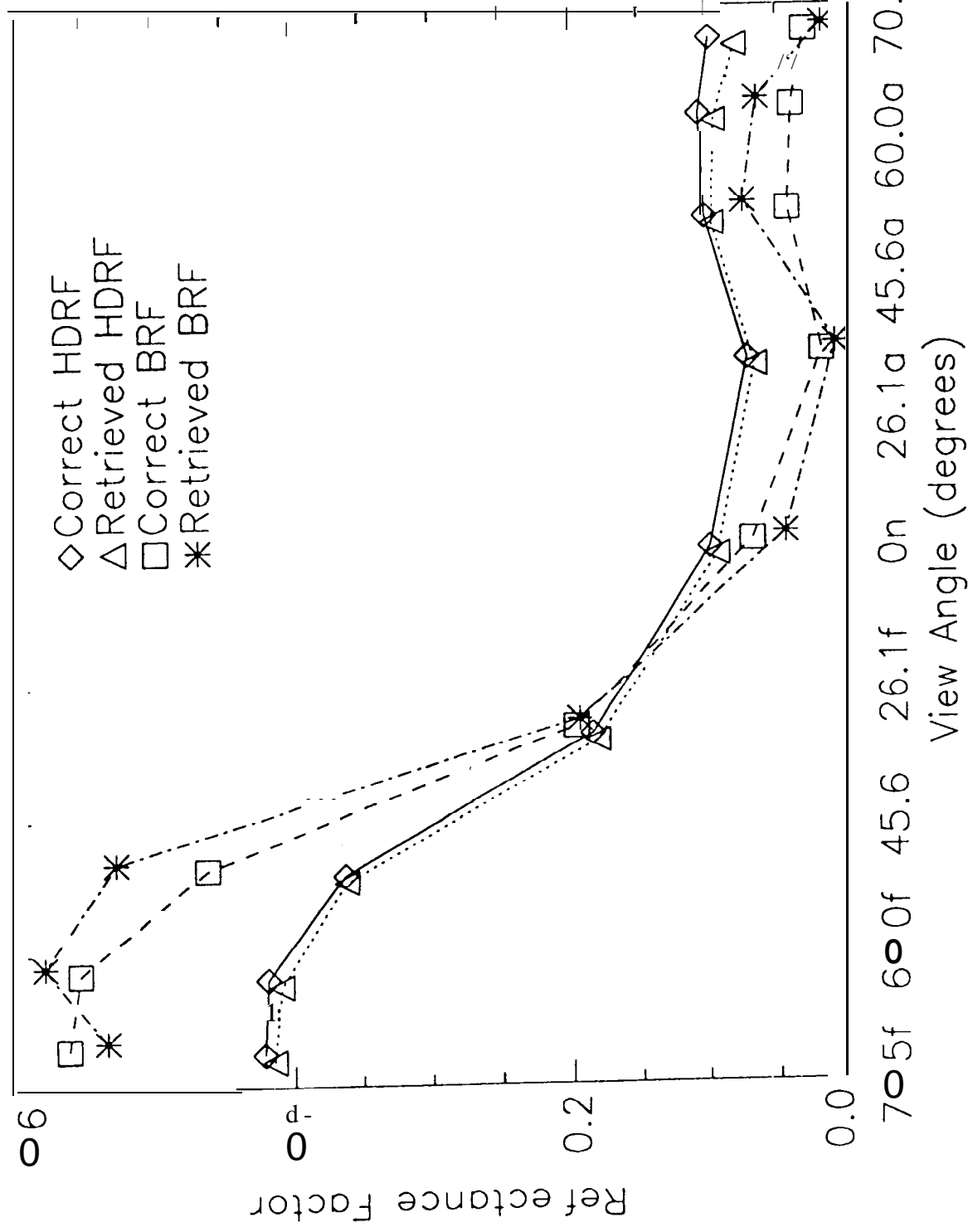


Figure 1





Soil



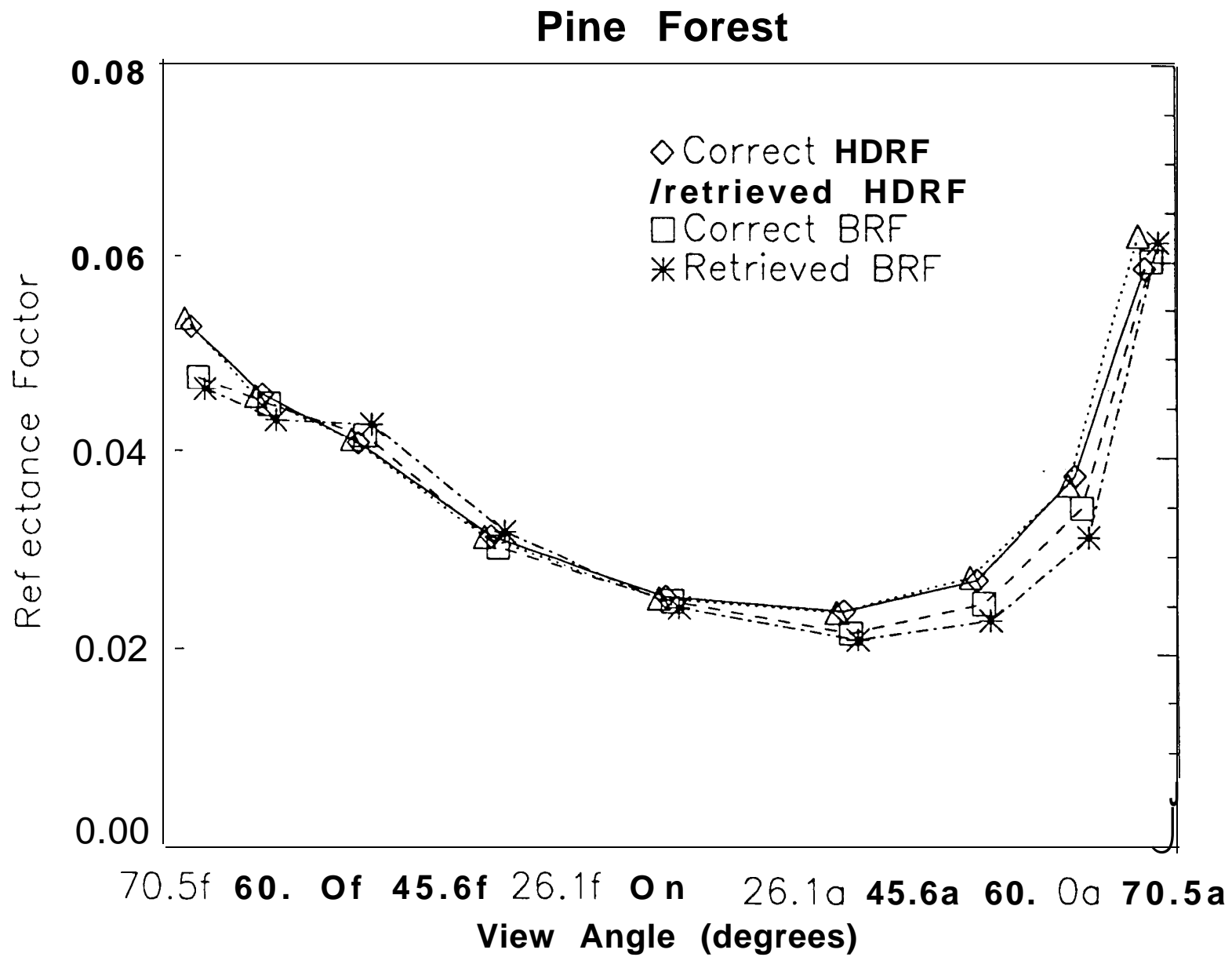
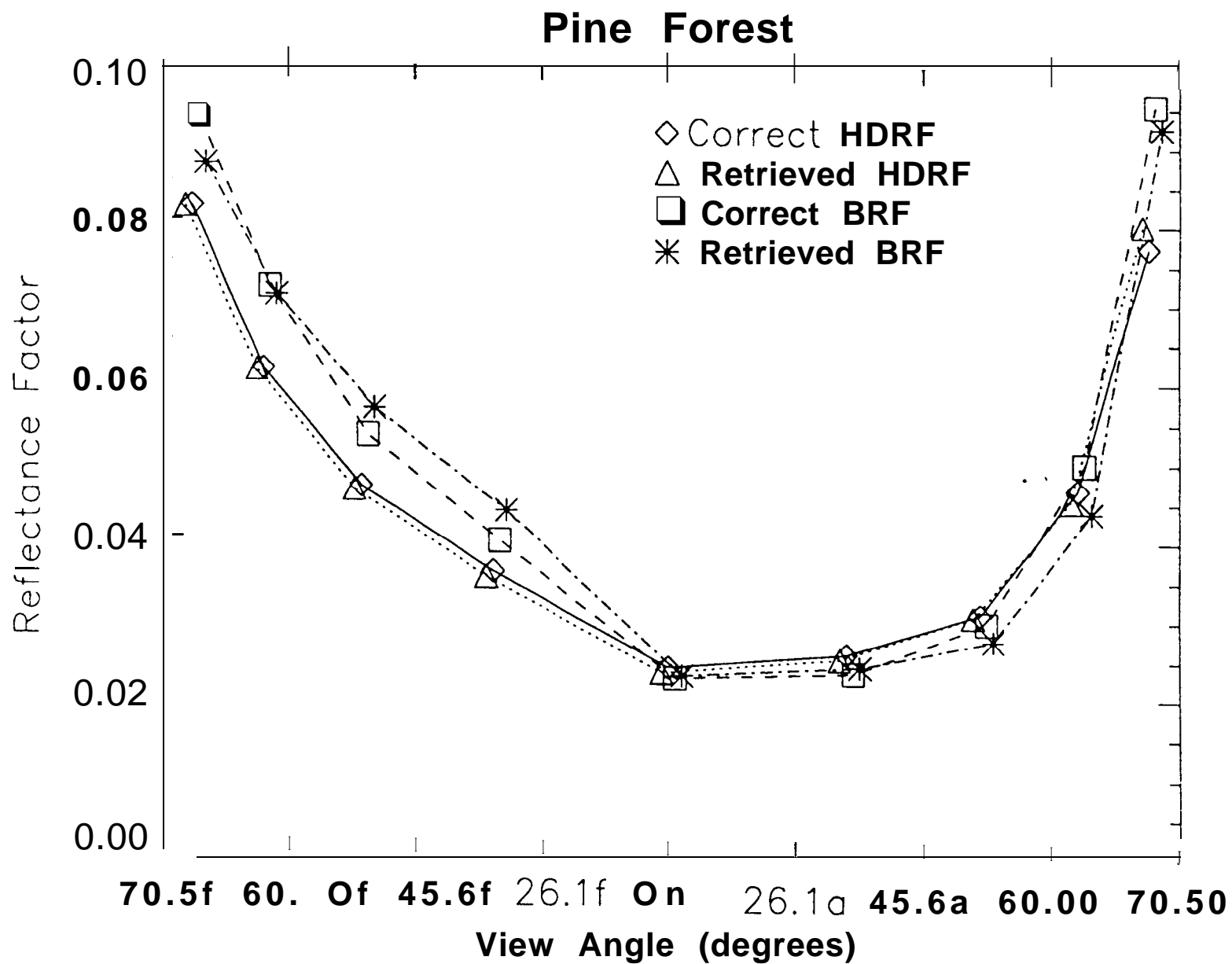
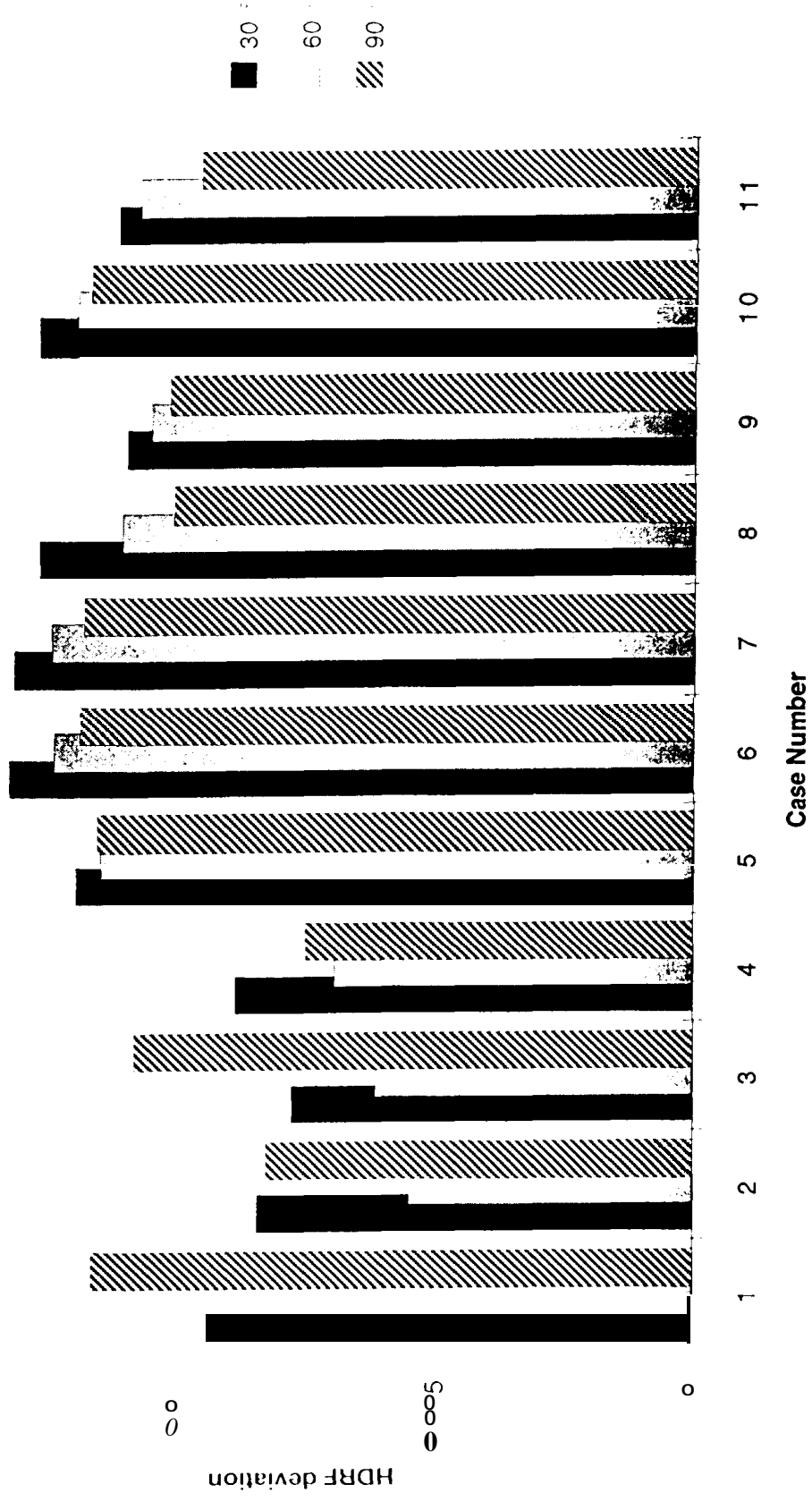
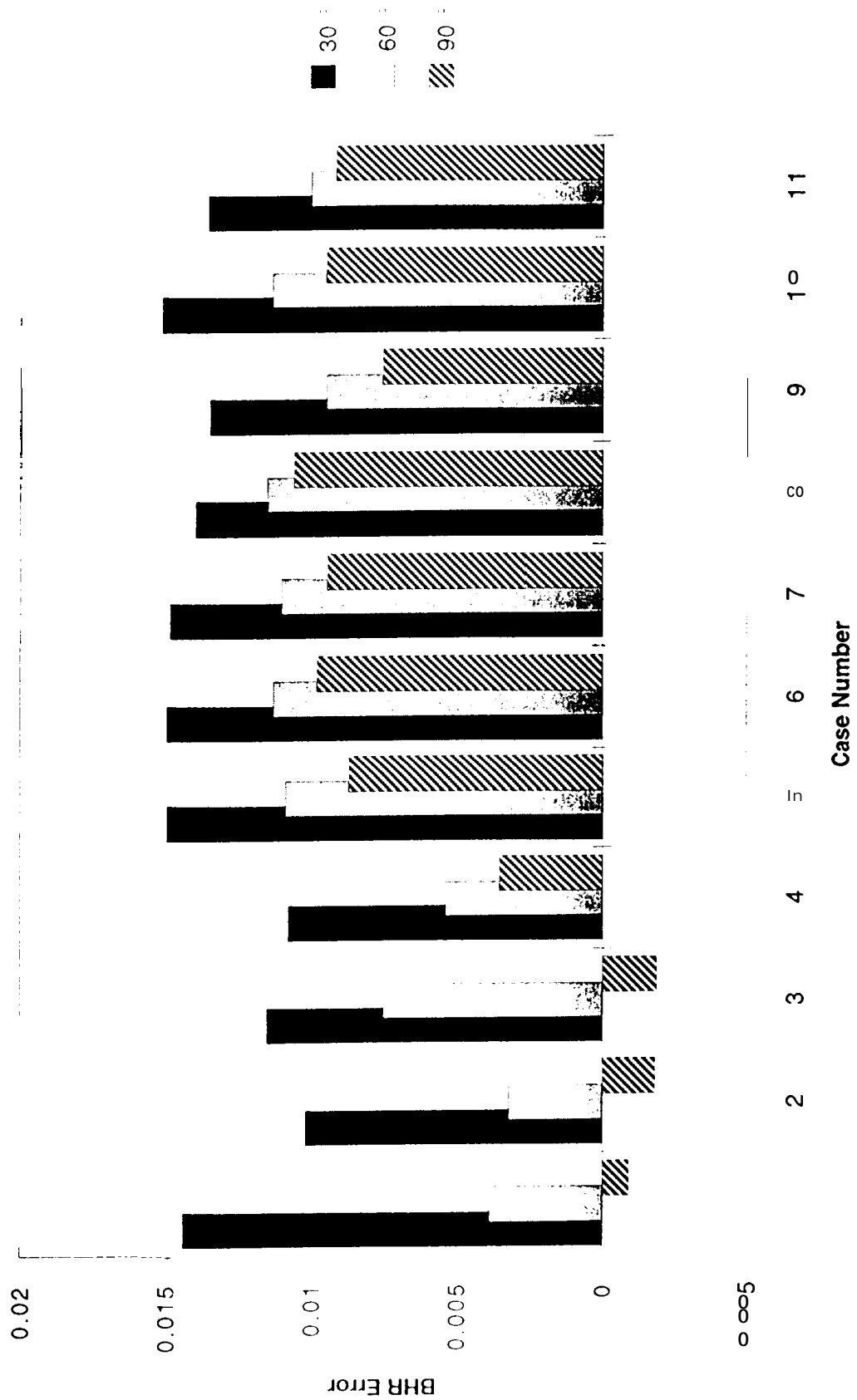


Figure 5



0.015





0.025

0.02

0.015

0.01

0.005

0

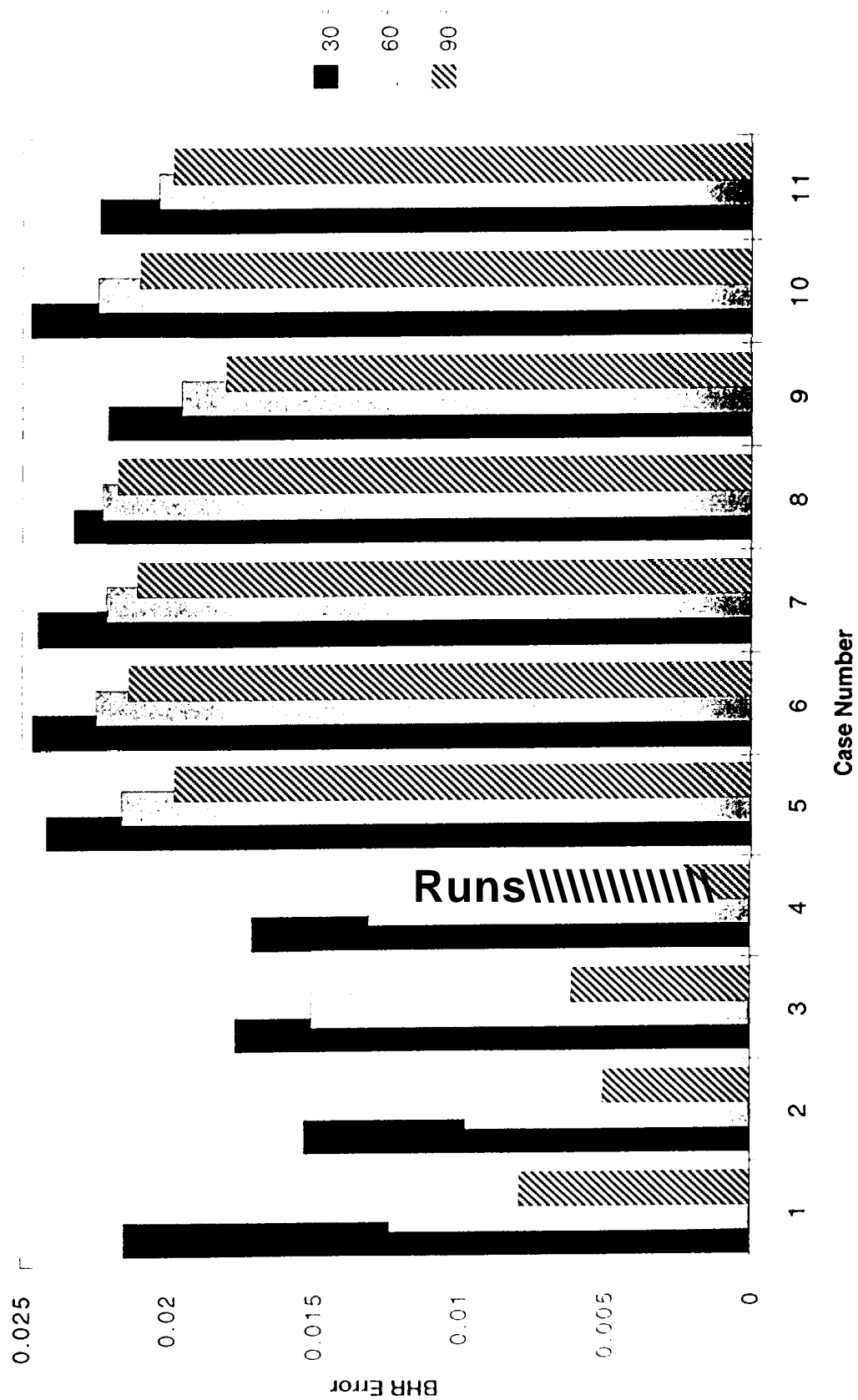
HDRF deviation

30°
60°
90°

1 2 3 4 5 6 7 8 9 10 11

Case Number

F 11.9



AUTHOR BIOGRAPHIES

John **V. Martonchik** received the B.S. degree in physics from Case Institute of Technology in 1964 and the Ph.D. degree in astronomy from the University of Texas at Austin in 1974. He joined JPL in 1972 and currently holds the position of Research Scientist. His experiences include telescopic and spacecraft observations of planetary atmospheres, laboratory and theoretical studies of the optical properties of gaseous, liquid, and solid materials, and development and implementation of one- and three-dimensional radiative transfer and line-by-line spectroscopy algorithms for studies of planetary atmospheres and Earth tropospheric remote sensing. He has been a Co-Investigator in several NASA programs and is the Algorithm Scientist for aerosol and surface retrievals on **MISR**.

David J. Diner received the B.S. degree in physics with honors from the State University of New York at Stony Brook in 1973 and the **M.S.** and Ph.D. degrees in planetary science from the California Institute of Technology in 1977 and 1978, respectively. He has been at the Jet Propulsion Laboratory since 1978, first as a National Research Council Resident Research Associate, then as a contractor with Ball Aerospace, and since 1981 as a JPL employee. He is currently a Member of the Technical Staff and Leader of the Multi-angle Imaging Science Element in the Earth and Space Sciences Division. He has been involved in numerous NASA planetary and Earth remote-sensing investigations, and is presently Principal Investigator of the EOS Multi-angle Imaging SpectroRadiometer (**MISR**) experiment and its airborne counterpart, **AirMISR**.

Bernard Pinty received his **Maîtrise de Chimie** and DEA (1977), *thèse de troisième cycle en Physique de l'Atmosphere* (1980) and *thèse d'Etat* (1988) from the **Université Blaise Pascal** in Clermont-Ferrand, France. He is presently affiliated with the Space Applications Institute (SAI) in Ispra, Italy. He visited the National Center for Atmospheric Research (NCAR) in Boulder, CO (198 S- 1989), served as Deputy Director of the **Laboratoire d'Etudes et de Recherches en Télédétection Spatiale (LERTS)** in Toulouse, France (1990- 1992), and was Professor of Physics at the University Blaise Pascal, France (1993- 1996). Dr. Pinty received the Zel'dovich medal from COSPAR (1990) and is a member of the MERIS Scientific Advisory Group of the European Space Agency and a **MISR** science team member. He serves as an Associate Editor for the Journal of Geophysical Research-Atmosphere. His main interests include research on the theory of radiation

transfer in plant canopies and, more generally, the development of tools to quantitatively interpret satellite remote sensing data in the solar spectral domain.

Michel M. Verstraete received his License en Physique (1974) from the Université Catholique de Louvain in Louvain-la-Nueve, Belgium, his License Spéciale en Géophysique (1976) from the Université Libre de Bruxelles, Belgium, and both his M. SC. in Meteorology (1978) and D. SC. in Atmospheric Sciences (1985) from the Massachusetts Institute of Technology in Cambridge, MA. He worked for the World Meteorological Organization in Geneva, Switzerland and Nairobi, Kenya from 1979-1981, at the National Center for Atmospheric Research (NCAR) in Boulder, CO from 1982-1989, taught at the University of Michigan in Ann Arbor from 1989-1990, and is currently employed at the Space Applications Institute (SAI) in Ispra, Italy. He is a member of various scientific advisory committees of the European Space Agency (e.g., MERIS) and is a MISR science team member. His initial work on topics such as the modeling of atmosphere-biosphere interactions and desertification led him to his current interest in the quantitative exploitation of satellite remote sensing data for the detection and characterization of terrestrial surface properties.

Ranga B. Myneni obtained his Ph.D. in Biology from the University of Antwerp in Belgium in 1985. Since then, he has worked at Kansas State, the University of Gottingen and NASA Goddard Space Flight Center. He is now an Associate Professor in the department of Geography at Boston University. His research interests are radiative transfer, remote sensing of vegetation and climate-vegetation dynamics. He is a member of the MODIS and MISR science teams.

Yuri Knyazikhin received [he M.S. degree in applied mathematics from Tartu University, Estonia, and the Ph.D. degree in numerical analysis from the N.I. Muskhelishvili Institute of Computing Mathematics, the Georgian Academy of Sciences, Tbilisi, Georgia, in 1978 and 1985 respectively. From 1978 to 1990 he was a Research Scientist at the Institute of Astrophysics and Atmospheric Physics and Tartu University (Estonia), Computer Center of the Siberian Branch of the Russian Academy of Sciences. He was an Alexander von Humboldt Fellow from 1992 to 1993, and worked at the University of Goettingen, Germany ([990- 1996). He is currently a Research Associate Professor in the Department of Geography at Boston University. He has worked and published in areas of numerical integral and differential equations, theory of radiation transfer in atmospheres and plant canopies, remote sensing of the atmosphere and plant canopies, ground-

based radiation measurements, forest ecosystem dynamics and modeling sustainable sociate Professor in the Department of Geography at Boston University. He has worked and published in areas of numerical integral and differential equations, theory of radiation transfer in atmosphere and plant canopies, remote sensing of the atmosphere and plant canopies, ground-based radiation measurements, forest ecosystem dynamics and modeling sustainable multifunctional forest management.

Howard R. Gordon is Professor of Physics at the University of Miami. He received the B.S. degree in physics from **Clarkson College of Technology** (now **Clarkson University**) in 1961 and the **M.S.** and **Ph.D.** degrees in physics from the Pennsylvania State University in 1963 and 1965, respectively. In 1975 he became a member of the Nimbus-7 Coastal Zone Color Scanner (**CZCS**) experiment team --- the first satellite instrument designed to study the variability in the distribution of phytoplankton in the ocean. He was awarded the Public Service Medal by NASA in 1982 for the development of methods for recovering **phytoplankton** pigment concentrations from **CZCS** imagery. He is presently a *science* team member of a number of new satellite instruments designed for a long-term assessment of global climate: the Sea-viewing Wide-Field-of-View Sensor (**SeaWiFS**), a **CZCS** follow-on to globally monitor the concentration of marine **phytoplankton**, launched August 1, 1997; the Moderate Resolution Imaging Spectroradiometer (**MODIS**) to be launched in 1998; and the Multi-angle Imaging **SpectroRadiometer** (**MISR**) to be launched in 1998. He was elected Fellow of the Optical Society of America in 1977, and has served as the Oceanic Optics Topical Editor of *Applied Optics*.